SANDIA REPORT

SAND97–0816 • UC–700
Unlimited Release
Printed April 1997

Inductive Voltage Adder Advanced Hydrodynamic Radiographic Technology Demonstration

M. G. Mazarakis, J. W. Poukey, J. E. Maenchen, D. C. Rovang, P. R. Menge, D. L. Smith, J. A. Halbleib, S. R. Cordova, L. Bennett, K. Mikkelson, R. Pepping, W. A. Stygar, T. G. Trucano, D. R. Welch, T. J. T. Kwan, B. G. DeVolder, R. J. Kares, C. M. Snell

Prepared by
Sandia National Laboratories
Albuquerque, New Mexico 87185 and Livermore, California 94550

Sandia is a multiprogram laboratory operated by Sandia Corporation, a Lockheed Martin Company, for the United States Department of Energy under Contract DE-AC04-94AL85000.

Sandia National Laboratories

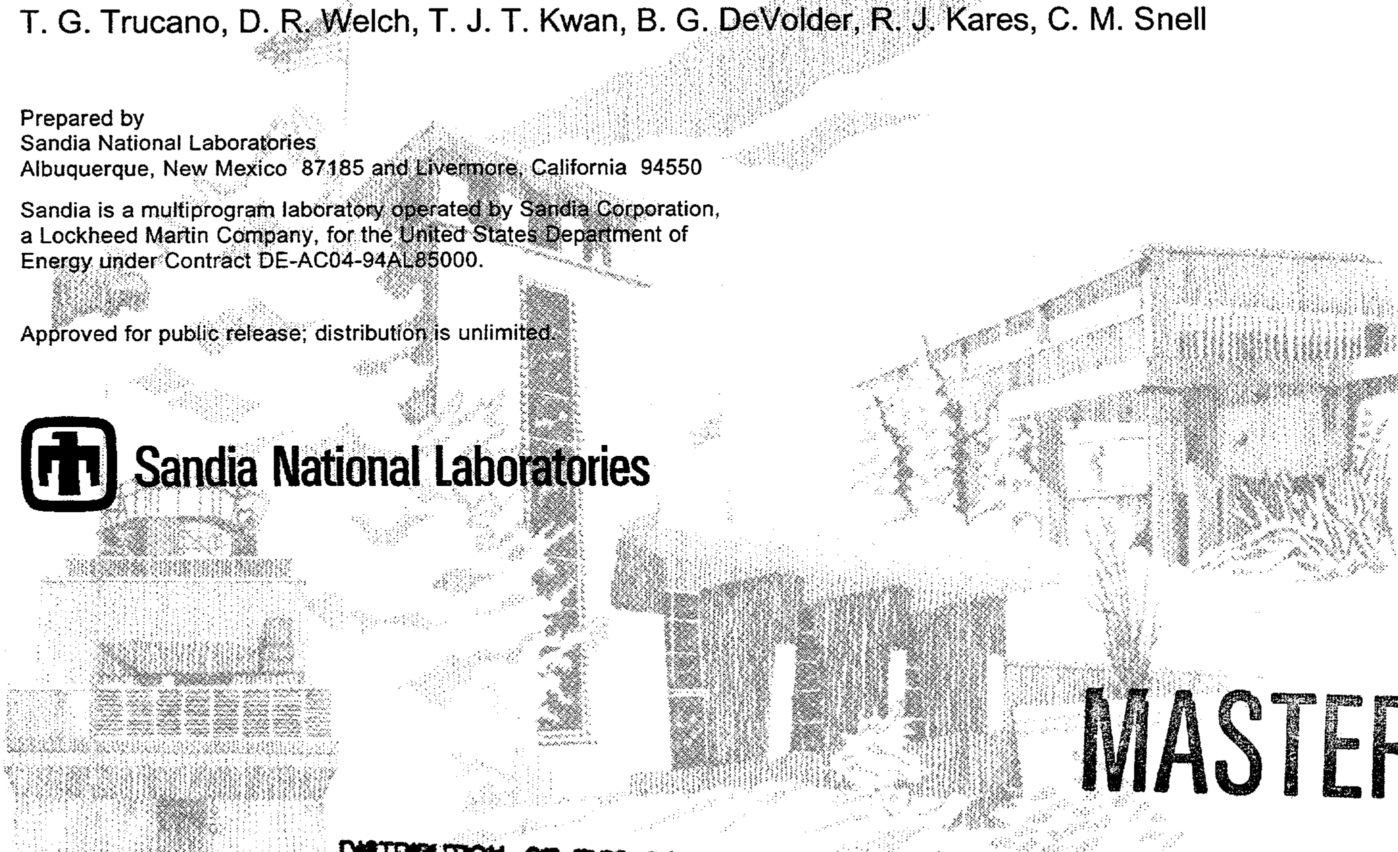

SF2900Q(8-81)

Issued by Sandia National Laboratories, operated for the United States Department of Energy by Sandia Corporation.

Printed in the United States of America. This report has been reproduced directly from the best available copy.

Available to DOE and DOE contractors from
Office of Scientific and Technical Information
P.O. Box 62
Oak Ridge, TN 37831

Prices available from (615) 576-8401, FTS 626-8401

Available to the public from
National Technical Information Service
U.S. Department of Commerce
5285 Port Royal Rd
Springfield, VA 22161

NTIS price codes
Printed copy: A04
Microfiche copy: A01

SAND97-0816
Unlimited Release
Printed April 1997

Distribution
Category UC-700

Inductive Voltage Adder Advanced Hydrodynamic Radiographic Technology Demonstration

M. G. Mazarakis, J. W. Poukey, J. E. Maenchen, D. C. Rovang, P. R. Menge, D. L. Smith, J. A. Halbleib, S. R. Cordova, L. Bennett, K. Mikkelson, R. Pepping, W. A. Stygar, and T. G. Trucano
Sandia National Laboratories, P. O. Box 5800, Albuquerque, NM 87185-1193

D. R. Welch
Mission Research Corporation, Albuquerque, NM 87106

T. J. T. Kwan, B. G. DeVolder, R. J. Kares, and C. M. Snell
Los Alamos National Laboratory, Los Alamos, NM 87545

Abstract

This paper presents the design, results, and analysis of a high-brightness electron beam technology demonstration experiment completed at Sandia National Laboratories, performed in collaboration with Los Alamos National Laboratory. The anticipated electron beam parameters were: 12 MeV, 35-40 kA, 0.5-mm rms radius, and 40-ns full width half maximum (FWHM) pulse duration. This beam, on an optimum thickness tantalum converter, should produce a very intense x-ray source of ~ 1.5-mm spot size and 1 kR dose @ 1 m. The accelerator utilized was SABRE, a pulsed inductive voltage adder, and the electron source was a magnetically immersed foilless electron diode. For these experiments, SABRE was modified to high-impedance negative-polarity operation. A new 100-ohm magnetically insulated transmission line cathode electrode was designed and constructed; the cavities were rotated 180° poloidally to invert the central electrode polarity to negative; and only one of the two pulse forming lines per cavity was energized. A twenty- to thirty-Tesla solenoidal magnet insulated the diode and contained the beam at its extremely small size. These experiments were designed to demonstrate high electron currents in submillimeter radius beams resulting in a high-brightness high-intensity flash x-ray source for high-resolution thick-object hydrodynamic radiography.

The SABRE facility high-impedance performance was less than what was hoped. The modifications resulted in a lower amplitude (9 MV), narrower-than-anticipated triangular

voltage pulse, which limited the dose to ~ 20% of the expected value. In addition, halo and ion-hose instabilities increased the electron beam spot size to > 1.5 mm. Subsequent, more detailed calculations explain these reduced output parameters. An accelerator designed (versus retrofit) for this purpose would provide the desired voltage and pulse shape. An improved MITL-to-diode transition region design together with additional shaping of the solenoidal fringe field should eliminate the halo. The ion-hose instability was found to saturate and the x-ray source size should therefore be further reduced by electrode cleaning, the use of a stronger 35-40 T magnet, and a smaller anode-cathode (AK) gap.

Thus, the technology demonstration effort began with a theoretical model predicting that inductive voltage adder driven x-ray sources should scale to the high-brightness, small-spot parameters critical for advanced hydrodynamic radiography. The SABRE experiment both discovered unanticipated technology limitations and, guided by improved modeling and simulation understanding, demonstrated engineering solutions. The experimental results validate the improved prediction tools and provide a solid data point scaling to full Advanced Hydrodynamic Radiographic parameters, successfully demonstrating the technology.

Acknowledgments

We thank Roger Fischer, DP-10, Bob DeWitt, DP-16, Don Cook, Jim Powell, and the Sandia National Laboratories National Security Sector for their support and encouragement.

Contents

I. Introduction 5
II. SABRE Modifications 5
III. High-Impedance MITL Design 7
IV. Diode Design 10
V. Power Flow Simulations 11
VI. Immersed Diode Parameter Sensitivity Simulations 14
A. AK Gap (d) 14
B. Cathode Radius (r_K) 15
C. Ion Effects 15
D. Applied B 16
VII. IVORY Streaming Instability Modeling 19
VIII. 3D Beam Formation Asymmetry Calculations 21
IX. Target Hydrodynamic Response 22
X. SABRE Accelerator and Diode Performance 28
XI. Diagnostics and Experimental Results 29
A. Current Measurements 31
B. Voltage Measurements 34
C. Prepulse 34
D. Beam Transverse Velocity ($\beta_\perp$) and Dose Measurements 37
E. Beam Spot Size 40
XII. Summary 45
References 47

DISCLAIMER

Inductive Voltage Adder Advanced Hydrodynamic Radiographic Technology Demonstration

I. Introduction

During the last 15 years, Sandia National Laboratories dedicated a considerable effort toward developing ultra high-current and high-brightness electron beams from 4 to 20 MeV and 30 to 100 kA. The accelerators utilized were compact and inexpensive single pulse devices, which can be divided into two groups: single stage Blumleins such as HERMES II[1] and IBEX,[2] and multistage devices such as RADLAC I,[3] RADLAC II,[4] RADLAC II/SMILE,[5] and MABE.[6]

The electron source used in these experiments was the magnetically immersed foilless diode,[7] where high-current and high-brightness electron beams are generated and propagated in a strong axial magnetic field, and high currents can be contained in small radial cross sections with relatively small transverse velocities. The primary advantages of this source, in comparison to magnetic field free devices (such as the DARHT injector[8]), are its insensitivity to voltage and applied magnetic field variations and its production of high-current, small-radius electron beams in equilibrium, as opposed to beams focused at only one axial location.

The experiments were motivated by the success of converting RADLAC II (an induction linac) into an equal impedance (~ 120 ohm) inductive voltage adder coupled to a magnetically immersed foilless diode (RADLAC II/SMILE). High-quality, 13-MeV, 50-100 kA, 1-cm radius annular electron beams were produced with very sharply defined 2-3 mm thick annuli and low transverse velocities ($\beta_\perp \approx 0.05$).

The experiments described here utilized the SABRE[9] accelerator as a test bed modified to a higher impedance voltage adder (~ 120 ohm) driving a foilless diode immersed in a very strong (20-30 Tesla) solenoidal magnetic field. A tantalum bremsstrahlung converter is immersed in the same magnetic field and defines the anode of the diode.

In the next sections, the SABRE modifications, the magnetically immersed foilless diode, numerical simulation predictions, and analysis of the experimental results are presented.

II. SABRE Modifications

The SABRE accelerator (Fig. 1) is based on the successful HERMES-III[10] technology developed at Sandia during the last ten years in collaboration with Pulse Sciences Inc.

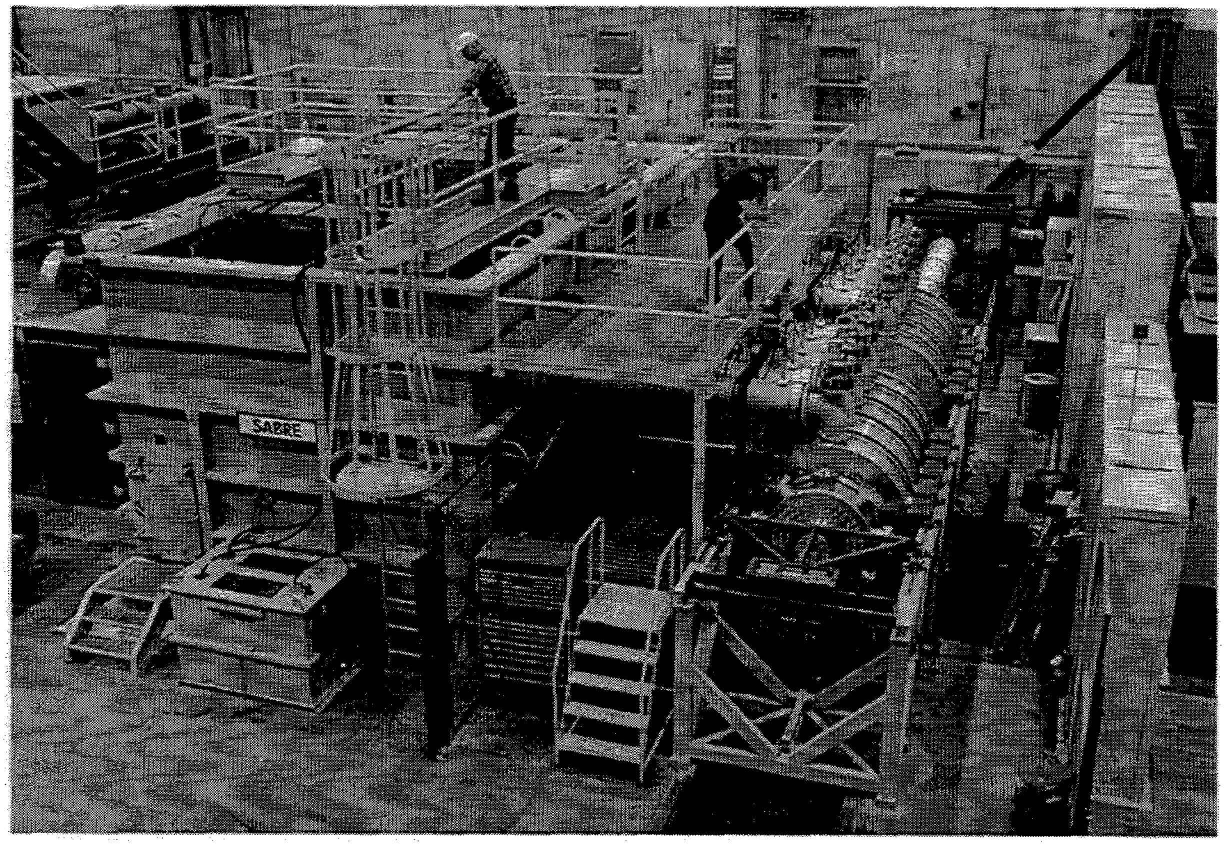

Figure 1. Sandia Accelerator for Beam Research (SABRE).

This technology is relatively simple and couples a self-magnetically insulated transmission line (MITL)[11] with an induction linac[12] to generate a new family of induction accelerators, which we call inductive voltage adders. In these accelerators, the particle beam which drifts through the multiple cavities of conventional induction linacs is replaced by a metal conductor which extends along the entire length of the device. The voltage addition of the accelerating cavities is therefore accumulated in the TEM Poynting vector rather than in a sequentially accelerated electron beam. These devices can operate in either polarity to produce negative or positive voltage pulses. In a negative polarity voltage adder (Fig. 2), the center conductor is negatively charged relative to the outer conductor which is interrupted at regular intervals by the cavity gaps. SABRE has 10 inductively insulated cavities each rated at 1.2 MV, designed to operate at 40 ohms in negative polarity and at 20 ohms in positive polarity. Ideally, SABRE should produce -12 MV, 300 kA, and +8 MV, 400 kA. Because of higher than expected energy losses in the pulse forming network, the operating input cavity voltage is 800 kV which limits the total output voltage to ~ 8 MV for negative polarity and 6 MV for positive polarity.

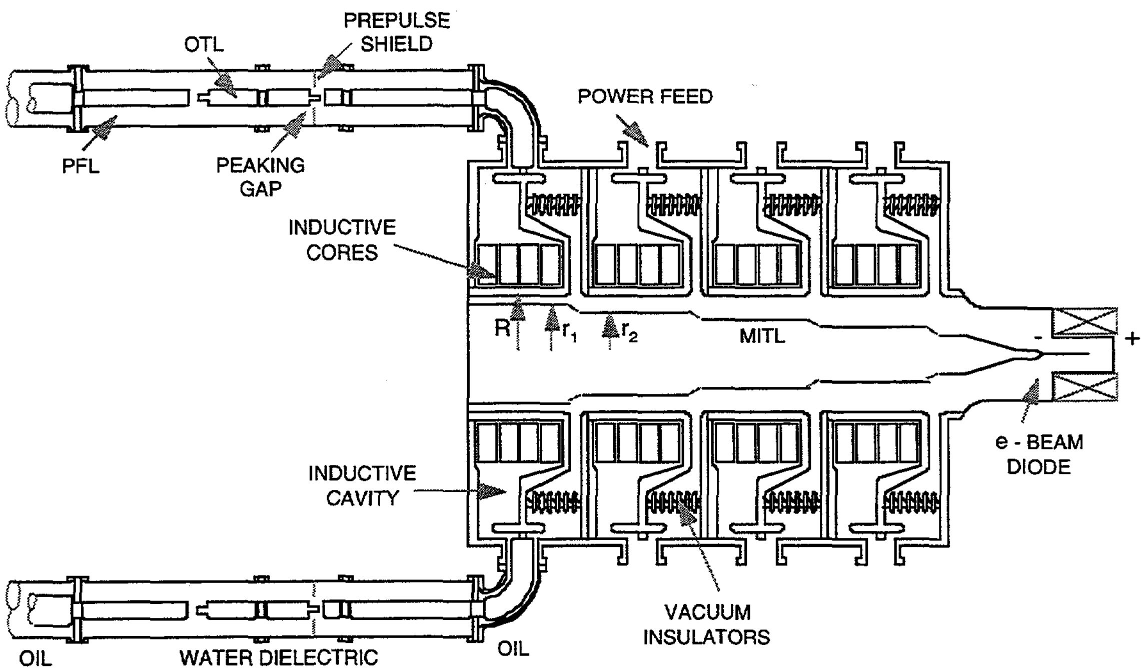

Figure 2. A negative polarity voltage adder of the SABRE type.

SABRE was, therefore, modified to increase the output voltage and proportionally reduce the current, delivering the same total energy. SABRE's slow pulsed power section consists of a Marx generator, two intermediate storage capacitors, and two triggered gas switches. Each switch controls the charging of ten pulse forming lines (PFLs). The PFLs charge as capacitors but discharge through self breaking water switches as 7.8-ohm, 40-ns transmission lines, each pair driving a cavity through a bent output transmission line structure (Fig. 2). This fast pulsed power section was modified by halving the number of pulse forming and transmission lines (from 20 to 10), feeding each cavity only from one side.

Halving the fast pulsed power section substantially increased the intermediate store-pulse forming line ringing ratio, providing a 50% higher voltage to the transmission lines and cavities (~ 1.2 MV). To take advantage of and to maintain the voltage gain, the voltage adder impedance was also increased by constructing a smaller diameter cathode electrode. Normally, the impedance of the voltage adder is matched to that of the cavities; however, to maintain a margin for further increasing the output voltage, the voltage adder impedance was built 40% higher. The transfer switches were adjusted to close at 2.2 MV, instead of the usual 2.6 to 2.8 MV, to avoid exceeding 1.2 MV per cavity.

III. High-Impedance MITL Design

The high-impedance voltage adder was designed utilizing Creedon's formalism,[11] for a pulse-forming-line-fed self-magnetically insulated transmission line system performing a series addition of voltage pulses from 10 cavity gaps (feeds). The cathode is a stepped geometry shown in Figs. 2 and 3. The constant radius segments provide constant vacuum impedance, and the impedance increases at a rate which follows the axial voltage gradient along the feed. The latter assures constant current flow over the entire length of SABRE and evanescent reverse directed electromagnetic waves.

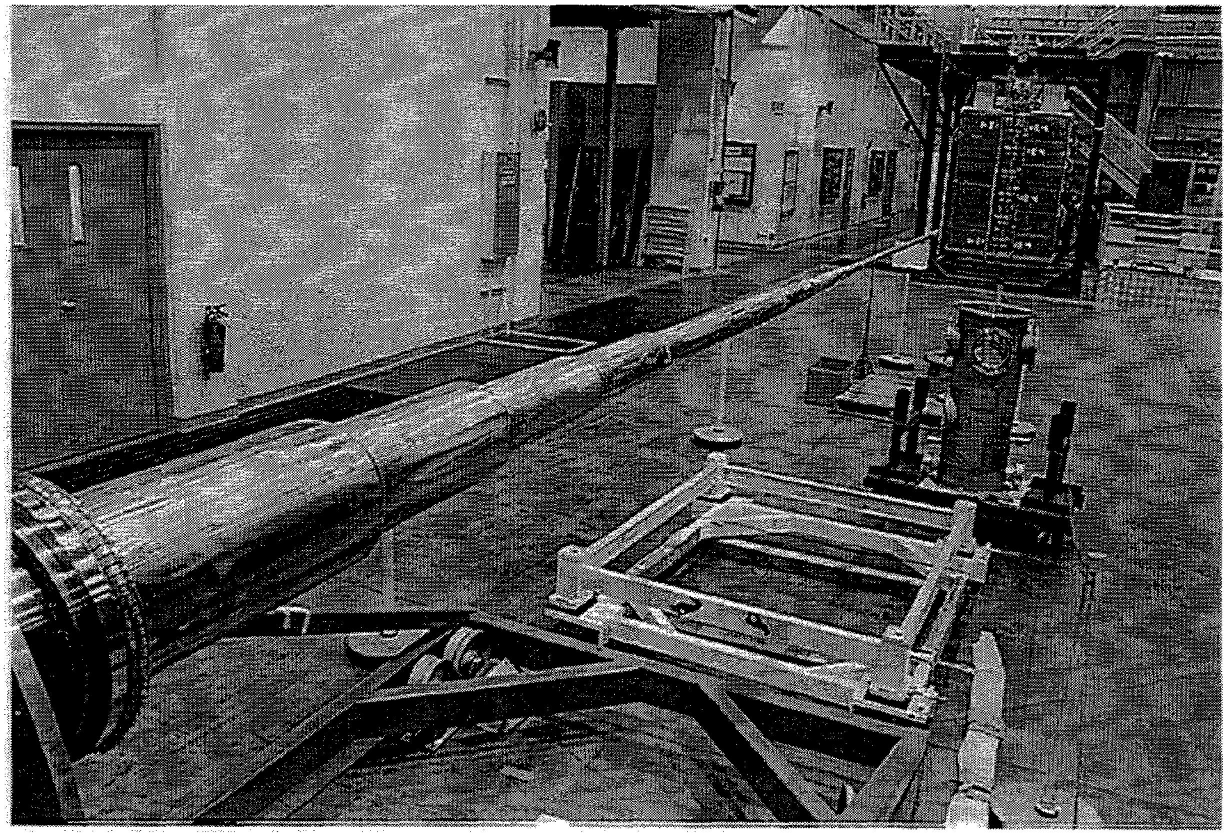

Figure 3. Photograph of the cathode electrode. The 12 segments are preloaded to compensate for the gravitational droop which is of the order of 20 cm.

The vacuum impedance Z_i of each section i depends only on the dimensions of Fig. 2 and can be easily calculated: $Z_i = 60 \ \ln(R/r_i)[\Omega]$; $i = 1,2, \ldots .10$, where R = 19 cm is the anode inner radius and r_i is the radius of the i-th cathode segment. A MITL does not, however, operate at this simple vacuum impedance as the trapped flow of electrons modifies the electromagnetic wave transport. The point design of 110 kA assumes equal 1.2 MV at each cavity feed. The operating impedance of each section is determined by the desired degree of overmatch of the MITL to the cavity feeds (~ 1.44) together with the constant current I_ℓ of the voltage adder required to establish self-limited magnetic insulation:

$$I_\ell = 8500 \ \ g\gamma_\ell^3 \ell n\left[\gamma_\ell + \left(\gamma_\ell^2 - 1\right)^{1/2}\right], \tag{1}$$

where $g = [\ln R/r_i]^{-1}$, $\gamma_i = V_i[\mathrm{MV}]/mc^2 + 1$, and γ_ℓ is the relativistic factor for electrons at the outer boundary of the electron sheath in the minimum current case, approximated by:[12]

$$\gamma_\ell \cong \frac{12\ \gamma_i^{1/3}}{12 + \ell n \left[\dfrac{\gamma_i}{5.9314}\right]} \tag{2}$$

Table 1 summarizes dimensions and design parameters chosen to maintain a constant I_ℓ throughout the accelerator. The cathode electrode in Fig. 3 (~ 9.6 m), including the voltage adder section (6 m long) and a constant radius extension section (3.6 m long), is cantilevered from the low voltage end of the accelerator. It starts with a 13.65-cm radius cylinder at the grounded end and tapers to 2.2-cm radius after the 10th cavity. Nine conical tapers were utilized along with 10 cylindrical sections and 11 flex-adjusting, double-washer sections preloaded to compensate for gravitational droop. Because of the large difference in radius between the surrounding anode and the cathode cantilever, precise alignment and centering is not critical since the electrical potential is a logarithmic function of the radii. Precise alignment is, however, required at the diode end, and the cantilevered cathode is adjusted *in situ* to center the high voltage end.

Table 1

Distance from cathode plate Z (cm)	Segment i (0 - 10)	Segment Voltage V_i (MV)	Cathode Radius R_c (cm)	Vacuum Impedance Z_i (Ω)	Operating Impedance Z_i (Ω)
0 - 33	0	0	13.65	20	11.6
37 - 80	1	1.2	13.65	20	11.6
84 - 127	2	2.4	10.95	33.2	22.6
131 - 174	3	3.6	8.41	49.0	35.3
178 - 221	4	4.8	7.14	58.9	44.4
225 - 366	5	6.0	5.715	72.2	55.5
370 - 413	6	7.2	4.76	83.2	65.0
417 - 460	7	8.4	3.81	96.6	76.6
464 - 507	8	9.6	3.175	107.5	86.3
511 - 554	9	10.8	2.54	120.9	98.1
558 - 900	10	12.0	2.22	129.0	105.5

IV. Diode Design

The magnetically immersed foilless diode is similar to those of RADLAC II/SMILE and IBEX.[13] However, here the impedance and solenoidal magnetic field are both much larger. In addition, the cathode here is a needle on axis as shown in Fig. 2 unlike the annular diodes in RADLAC and IBEX. To generate millimeter-size beams, the diode must be immersed in 20-Tesla solenoidal fields[14,15,16] (Fig. 4). The electrodes are made of titanium for its strength, nonmagnetic, and large resistivity properties, allowing the pulsed magnetic field to penetrate without appreciable losses.

The pulsed solenoids were designed and constructed at Sandia, drawing upon the extensive inertial confinement fusion ion beam electromagnet experience. Four 20-Tesla solenoids were constructed for redundancy, which have performed remarkably well over 100 shots, each without any apparent deterioration. These solenoids are among the strongest ever built. The total magnetic energy stored is ~ 1.8 MJ in an 8-mH inductance, providing a working bore of 12 cm, 30 cm long. The fringe field shape is tailored by a 2-cm thick aluminum cylinder coaxially enclosing the entire diode assembly. The magnetic field profile and strength (Fig. 5) are in good agreement with Atheta[17] numerical predictions, within the estimated measurement errors of 10%. Most recently, two even higher magnetic field, 30-Tesla, coils were built. One was constructed with a new, very rigid wire and failed. The second reliably provided the higher fields on ~ 6 shots without damage.

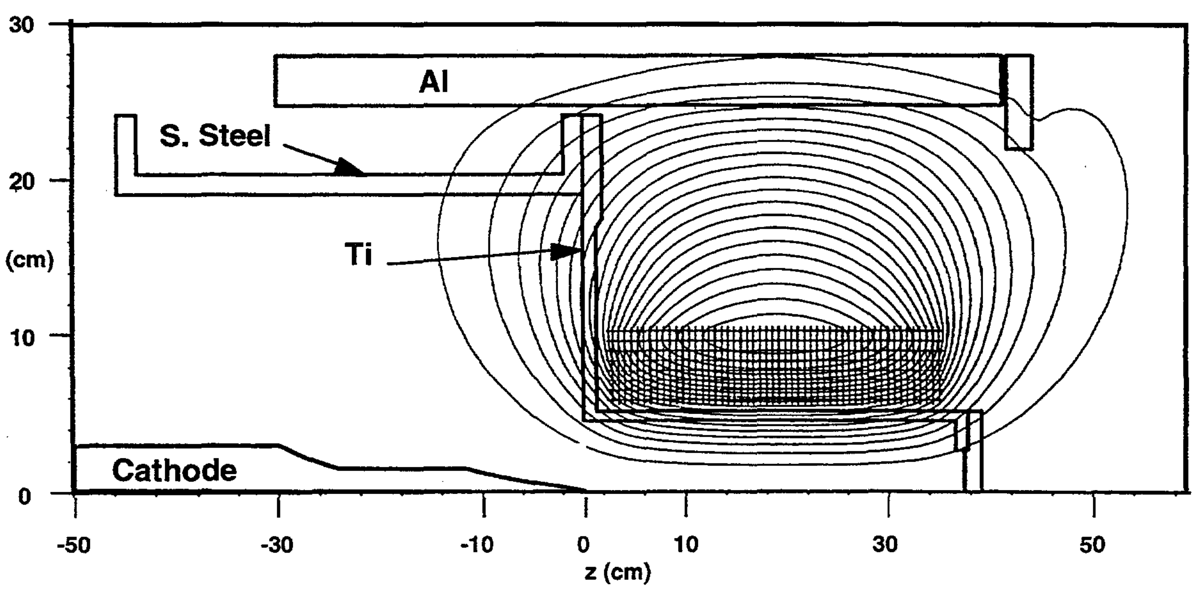

Figure 4. Schematic diagram of immersed diode design and transition region showing the applied magnetic field structure.

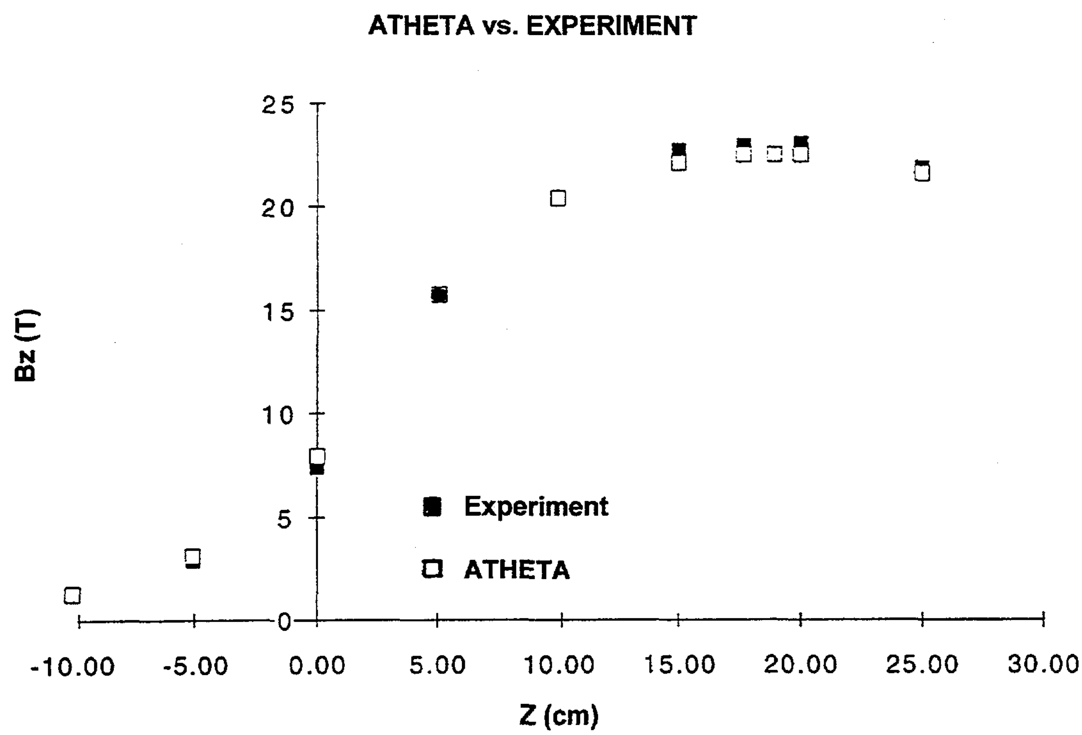

Figure 5. Measured and calculated magnetic field profile of the diode solenoid.

V. Power Flow Simulations

The design of the MITL voltage adder (Table 1) and the foilless diode[18] (Fig. 4) were validated with a large number of TWOQUICK[19] particle-in-cell simulations. Because of the large range in space and time scales, the entire design was divided into three parts: the voltage adder, from cavity feeds through the extension MITL to a self-limited diode load (Fig. 6); the transition region, where the coupling from the MITL into the immersed diode was studied (Fig. 7); and finally, the immersed diode where the beam generation and beam parameters were analyzed in fine detail (Fig. 8). The three simulations span the large scale of the entire SABRE voltage adder to the small scale of the immersed foilless diode and merge smoothly into one another.

Figure 6 shows an electron map at 60 ns following the arrival of the voltage pulse at the first cavity (t = 0). The line is magnetically insulated by the self-field (B_θ) of the current flowing through the voltage adder. Electron maps at earlier times (t = 20-30 ns) show the expected pulse front electron losses to the anode which initiates self-limited magnetically insulated flow. The simulated planar diode anode-cathode gap at the end of the MITL is large, 20 cm, to allow operation in the self-limited mode. No applied magnetic field is assumed. In this simulation, the cavity input voltage is the anticipated 1.2-MV trapezoidal pulse with a 40-ns flat top. Because the voltage adder is overmatched to the cavity impedance (12 ohm versus 7.8 ohm), the actual operating voltage pulse at the cavity gaps is higher, ~ 1.4 MV. These pulses combine and travel toward the slightly undermatched diode. The final voltage is 13 MV and the total current is 135 kA. The estimated operating impedance of 96 ohms agrees with the parapotential theory within 10%.

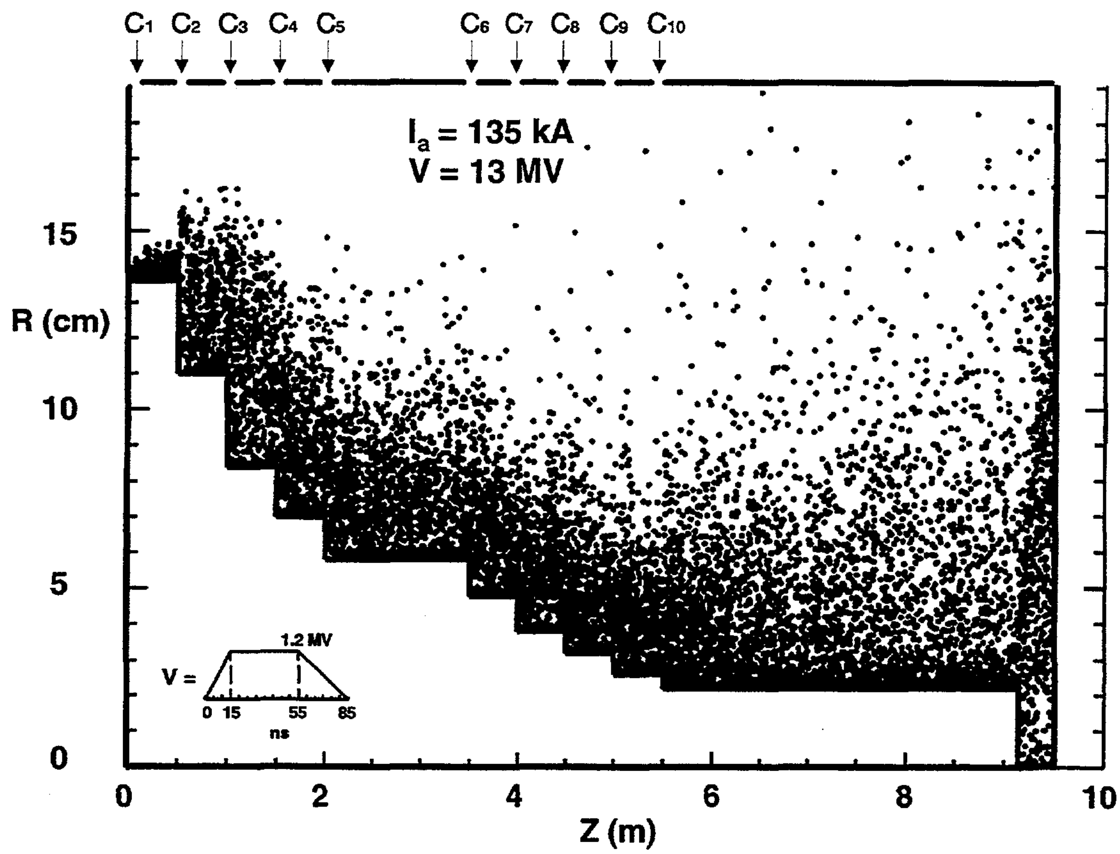

Figure 6. TWOQUICK PIC high-impedance negative MITL electron map 60 ns after voltage onset at the first cavity (t = 0).

Figure 7 is a simulation of the transition region where all the MITL sheath electrons are lost to the anode. The sum of the loss current and beam current is equal to the total current flowing along the voltage adder. Thus the transition region is the effective load for the SABRE MITL with an impedance equal to the MITL operating impedance (a matched load). The location of the cathode taper relative to the shape and strength of the solenoidal fringe field is critical. Figure 8 shows a configuration optimized for high brightness and low emittance. The radial electron losses near the conically tapered section are due to the B_r of the applied solenoidal magnetic field structure (shown) where the MITL self-field B_θ becomes equal to the B_Z component of the applied field. The current splits: about 70% flows radially to the graphite-lined MITL wall and the remaining 36 kA forms a pencil-like beam of about 0.6-mm radius. The resolution of the simulation is not fine enough to predict precise beam parameters.

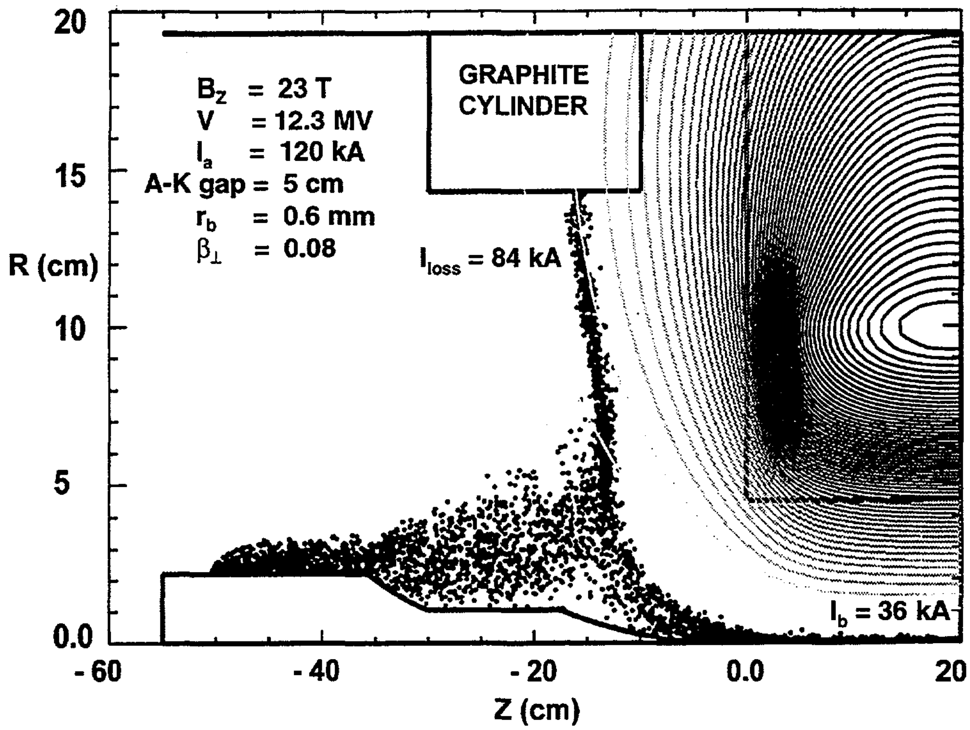

Figure 7. TWOQUICK PIC simulation of the transition region. The MITL sheath current is diverted to the anode where B_θ self-insulation (left side) transitions to applied B_Z insulation in the immersed diode ($0 < z < 20$ cm); see Fig. 8.

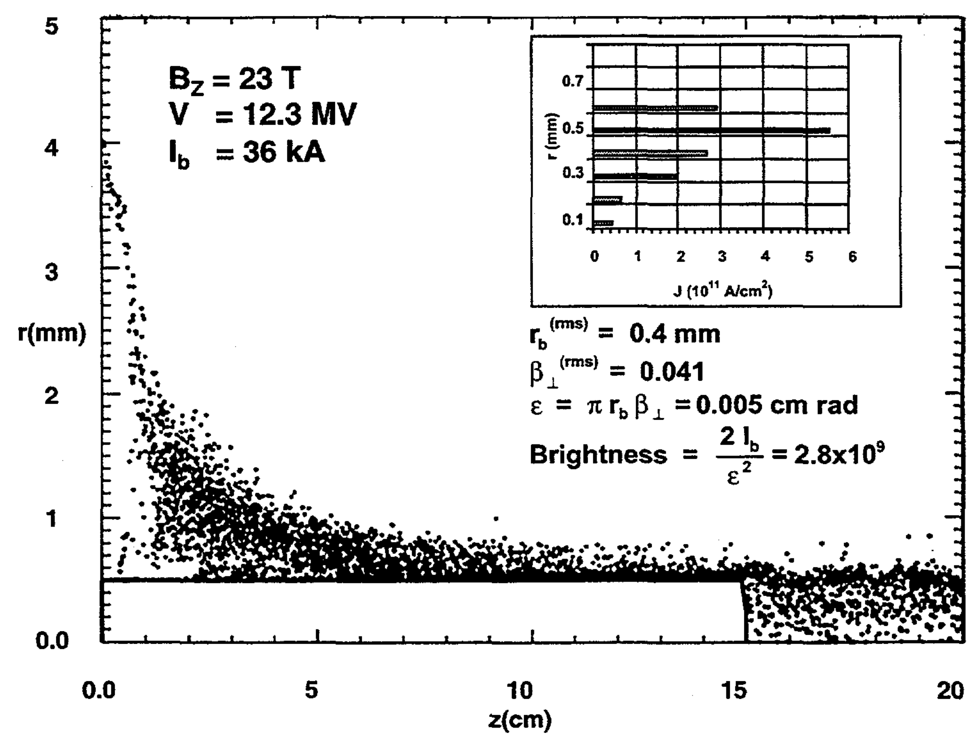

Figure 8. High-resolution TWOQUICK diode simulation calculating the beam parameters. Only the B_Z region of Fig. 7 is simulated. 36-kA of focused electron beam strikes the anode with 0.4-mm radius and $\beta_\perp \sim 0.04$.

The simulation of Fig. 8 was performed to address the above concern, finely resolving the immersed diode region. The modeled electrode boundaries and applied magnetic field match the experimental configuration, and the anode-cathode voltage applied is 12 MV. A beam of 36 kA with 0.44 mm rms radius is produced. This simulation represents an ideal situation assuming no cathode plasma radial expansion, perfect cylindrical symmetry without instabilities, and negligible beam perturbation due to possible target plasma expansion. The simulations predict a beam with emittance $\varepsilon = \pi r_b \beta_\perp = 5\times10^{-5}$ mrad. The brightness is $B = 2I/\varepsilon^2 = 3\times10^{13}$ A/(mrad)^2 where I is the beam current.

The simulated beams are very tightly focused which would strongly drive the target to superheated plasma conditions. For instance, the current density, power density, and energy density are, respectively, 5.5×10^6 A/cm^2, 6.0×10^{13} W/cm^2, and 2.4×10^6 J/cm^2. The target front surface dose is ~ 6×10^5 J/g, suggesting these beams could be used to investigate high-energy density physics issues at extreme conditions. This same target plasma and target debris expansion may have deleterious effects on the use of this electron beam for flash x-ray production, especially under a multipulsing regime.

VI. Immersed Diode Parameter Sensitivity Simulations

The previous section summarized the 2D power flow design coupling energy into a pencil electron beam. Three obvious issues are (1) parameter sensitivity, covered in this section, (2) 3D beam stability, covered in the following one, and (3) 3D asymmetries in beam formation (due to asymmetric cathode plasma expansion or machine irregularities) in the next section.

Parameter sensitivity is especially critical, since the goal is to generate a tiny beam and direct it precisely onto a carefully designed target. Large errors in magnetic-field coil position, for example, can generate an undesirable beam halo. On the other hand, the system appears robust to many parameters, suggesting the successful generation of a small beam on axis should be a realistic goal. Many parameter variations were studied; the few which seem most important are summarized below.

A. AK Gap (d)

The basic design has an anode-cathode (AK) axial spacing of d = 5 cm. Variations from 1-15 cm generate small effects in 2D (although they could provide more growth-length for instabilities in 3D). When the gap is increased to greater than 20 cm, however, the beam current I_b drops and the beam radius r_b and temperature $\beta_\perp$ increase. At d = 25 cm, for example, I_b = 25 kA, r_b = 1.6 mm, (almost triple the size of the design run; see Figs. 9 and 7), and $\beta_\perp$ = 0.16. Basically, this unrealistic case is where the needle-tip is removed. Since there is no advantage to using such a large gap, variations in AK gap should not present serious problems.

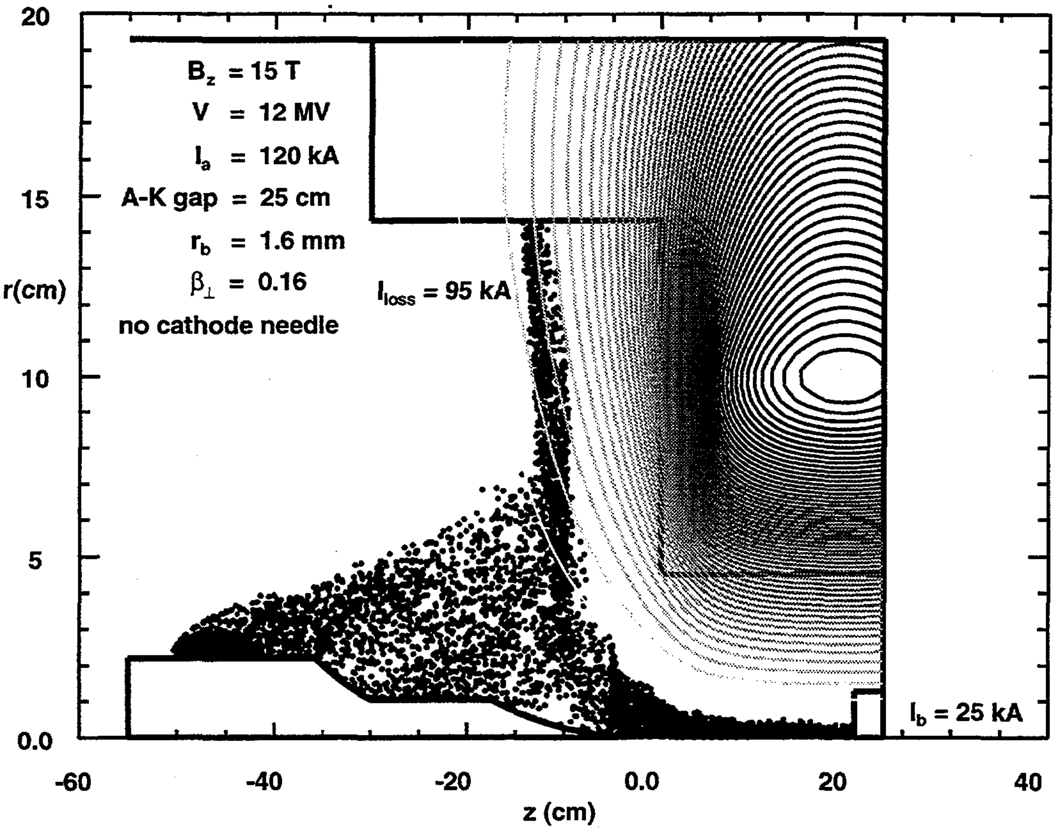

Figure 9. Very large gap (AK = 25 cm) PIC simulation of the transition region. There is no needle; the electrons are emitted from the conical needle holder. Beam current drops to 25-kA while the beam radius and temperature both nearly quadruple to 1.6 mm and $\beta_\perp$ = .16 (Compare Fig. 8).

B. Cathode Radius (r_K)

The result here is simple and expected: the beam size varies with cathode size: $r_b \approx r_K$. More precisely, without anode ion emission $r_b \leq r_K$. The beam current, I_b, of course, increases with r_K, but more slowly than linear. For example, increasing r_K to 5 mm (ten times the basic design) approximately doubles I_b (for fixed source impedance). The importance of this may be that if one could use a larger beam, it would probably be more stable (see Sec. VII). This configuration also provides a check on code (and experiment), since a broader database exists for larger beams.

C. Ion Effects

In 3D, it is possible that protons from the anode fundamentally limit the ability to finely focus the electron beam (see ion-hose section below), but in 2D the presence of ions actually improved performance. The ion space charge causes the electrons to pinch to a smaller radius (from r_b = 0.44 in Fig. 8 to 0.27 mm in Fig. 10), but also makes the beam hotter (from $\beta_\perp = 0.04$ to 0.19) and causes some rotation (β_θ [average] ≈ -0.1). This hollow rotating beam is subject to the diocotron instability, but the growth rate appears too small to pose a serious problem. In short, ions are only a major concern in 3D. In 2D, even ion emission from large anode areas did not significantly degrade performance.

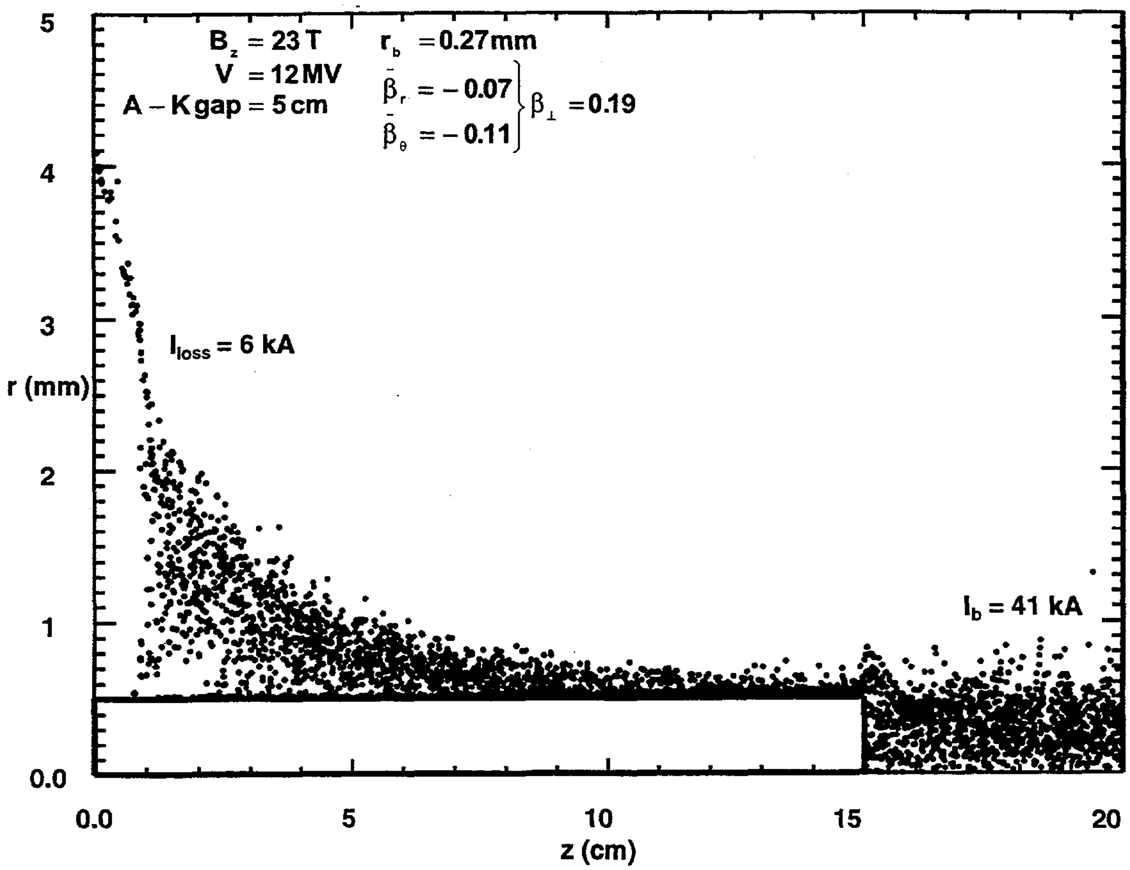

Figure 10. 2D PIC simulation including 1.2-kA backstreaming protons from the anode. Only the electrons are shown here. The presence of ion space charge causes the electrons to pinch to half radius (0.27 mm) in a five times hotter ($\beta_\perp = 0.19$) and rotating ($\beta_\theta = -0.1$) distribution; compare Fig. 8.

D. Applied B

Many variations in the applied magnetic field were studied, some crucial, some insignificant. Reducing the magnitude tends to increase both I_b and r_b; for example, reducing from 15 to 6 T (Fig. 11) increased I_b from 35 to 50 kA and r_b from 0.5 to 1.7 mm. Changing the B_Z profile by removing the Al cylinder (Fig. 4) is bad: even at 35 T the beam has $r_b = 1.7$ mm. Shifting the z-location of the coil by more than a few cm is even worse: a 10-cm shift toward the cathode results in a large halo at $r_b \approx 3$ mm carrying 2/3 of the beam current (Figs. 12a and b).

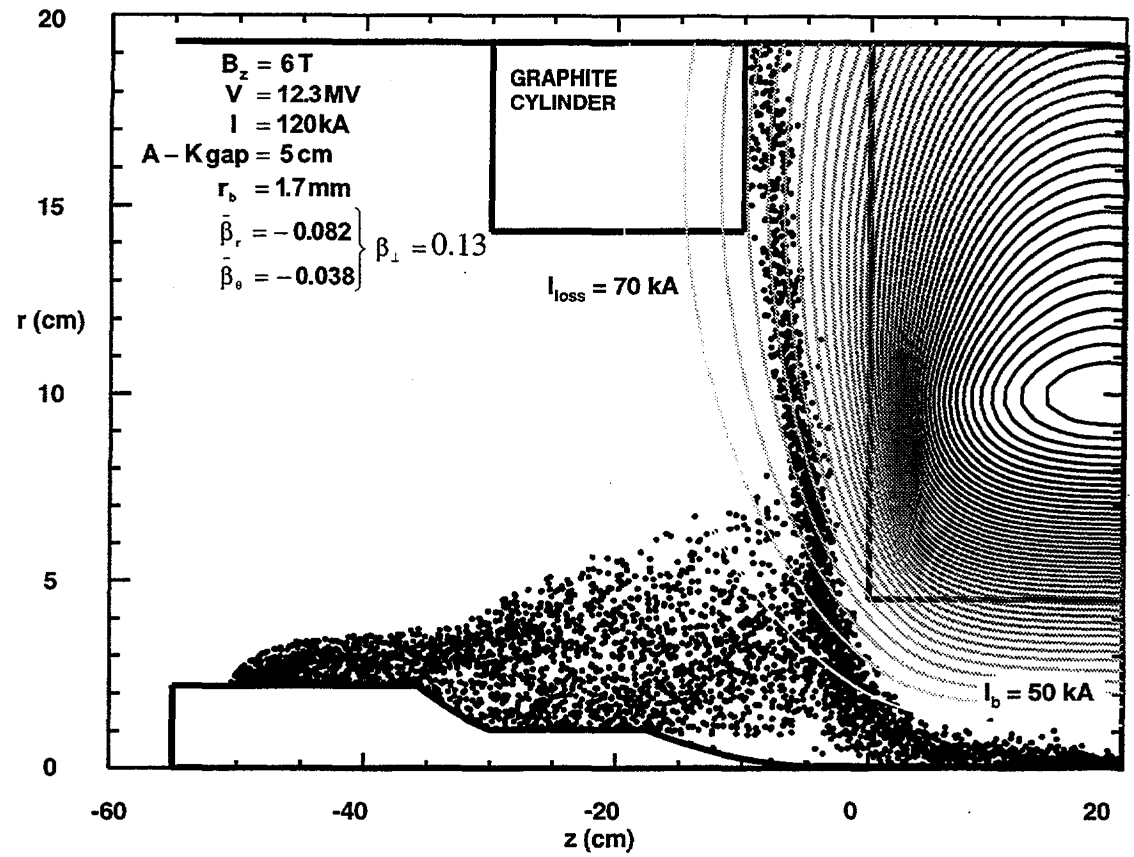

Figure 11. A lower magnetic field (6 T) can produce higher beam currents (50 kA); however, the radius is larger (1.7 mm) and the beam hotter ($\beta_\perp$ ~ .13).

(a)

(b)

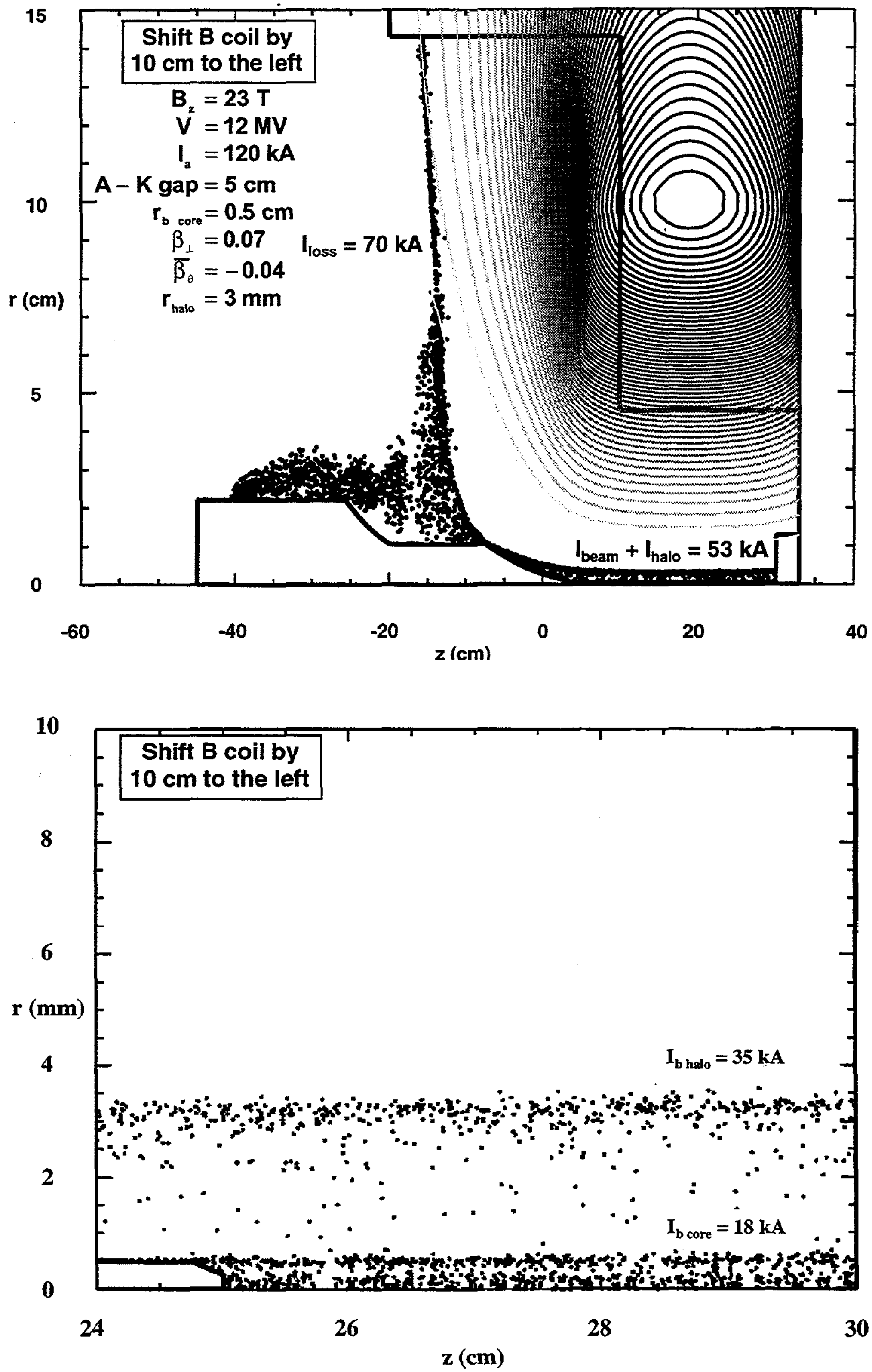

Figure 12. (a&b) A 10-cm axial displacement of the coil results in a large r_b = 2.6 mm beam with a halo conducting 2/3 of the beam current. Part (b) shows an expanded view of the gap region in part (a).

Somewhat surprisingly, changing the length of the coil from the standard 30 cm to shorter lengths is not a serious perturbation to the beam, provided the field maximum is near the center of the AK gap. For example, a 15-cm coil with B_Z (max) = 35 T yields I_b = 39 kA, r_b = 0.8 mm at 12 MV. The ultimate variation in this respect is a zero-length (single-turn) coil which gives (when properly centered) r_b = 0.6 mm, I_b = 30 kA at 35 T. The key here is that the B-fringe lines should curve away from the cathode stalk; if they curve toward it, the shank electrons emitted from the first cone can follow a B line and form a beam halo.

The sensitivity to voltage, cathode shape, and anode wall radii were considered during the design phase which resulted in the baseline experiment. Spot size is not sensitive to small changes (few MV) in voltage or to variations (few cm) in wall (anode) radius. Large changes in system impedance would, of course, necessitate a redesign.

Finally, it is important to note that all the above studies were steady-state results which should be appropriate so long as the experimental pulse has some flat top region. If the pulse is very triangular there is, strictly, no steady state, and some degradation in beam quality is expected. Sandia, Los Alamos, and MRC have performed simulations of the full SABRE diode system with similar assumed geometry and initial conditions. Detailed comparison of the results revealed gross similarity of behavior but some differences of detail. Specifically, the Los Alamos calculations produced a much larger beam radius and the phase space was somewhat more disperse than the corresponding Sandia results. Coarser zoning and longer time-steps in the Los Alamos simulations could explain some, but not all, of the observed deviation. Concerns arose that there might be serious numerical or physics inconsistencies among the PIC beam simulation codes. Therefore, an attempt was made to track down possible discrepancies among the major codes, TWOQUICK (Sandia), MERLIN (Los Alamos), and IVORY (MRC). This effort was rendered difficult by the complexity of the SABRE system and the large size of the calculations. However, the final outcome was simply that differences in the assumed external magnetic field caused most of the change in beam behavior.[20]

VII. IVORY Streaming Instability Modeling

The intense electron beam produced by the SABRE foilless diode quickly produces an ion-emitting anode plasma. The ions, likely protons, are accelerated toward the cathode with a current reduced roughly by the ratio of the ion-to-electron beam velocity (3 kA ions versus 30 kA electrons for typical SABRE parameters). The electrostatic attraction between the two beams is considerable and various forms of the two-stream instability are excited, including sausage, hollowing, hose, and filamentation. These instabilities can cause large deflections and heating of the beam which would increase the beam spot size in the absence of a strong axial magnetic field (B_Z).

Streaming instabilities, involving a beam in a comparable density plasma, typically have axial growth scale lengths proportional to the electron betatron wavelength. For a uniform density beam in a plasma channel of the same radius, $\lambda_\beta = 2\pi r_b(\gamma/2f\nu)^{1/2}$, where γ, ν, and f are the relativistic factor, beam current normalized to 17 kA, and the ratio of ion-to-beam line density, respectively. For a stationary ion column, the scale time for growth at a given axial position is proportional to the ion transverse slosh time, $\lambda_i = 2\pi r_b(m_i/2\nu m_e c^2)^{1/2}$. Theoretical and experimental research has found the ion-hose instability e-folds 4-6 times per λ_i. For the SABRE beam with 30 kA, 10 MeV, and 0.5-mm radius, $\lambda_\beta = 0.7$ cm and $\lambda_i = 0.2$ ns (protons). Thus, the instabilities can e-fold several times with a > 3-cm gap and > 1-ns pulse length. A strong B_z is effective at stabilizing hose growth in the nonlinear regime. A useful measure of such stabilization is the ratio of the beam radius to the Larmor radius r_b/r_l, which should be greater than or near unity to limit hose growth. Assuming the beam's transverse energy equals the ion space-charge potential, $\gamma\beta_\perp \doteq (2f\gamma\nu)^{1/2}$ the above condition suggests $B_Z > 0.17\, r_b^{-1} (2f\gamma\nu)^{1/2}$ for stability, or for SABRE parameters, $B_Z \geq 30$ Tesla, as a *rough* criterion.

The electron-ion instabilities have been modeled with the electromagnetic code IVORY.[21] The macroparticles are treated using particle-in-cell techniques. The two species, electrons and protons, are allowed to emit from the cathode and anode, respectively. Both axisymmetric and hose instabilities are examined by the Fouier decomposition of the currents and fields into m = 0, 1 and -1 azimuthal modes. The SABRE diode was simulated by launching a 6-MV voltage into a 5-cm outer radius diode with a 0.05-cm radius cathode stalk. With a 6-Tesla axial field, the hose instability caused the beam radius to grow from a 0.6-mm rms radius to 1.5 mm (Fig. 13). This growth was stabilized by increasing the axial field to 23 Tesla producing an acceptable 0.8 mm beam radius. These results confirm the simple theoretical scaling and suggest that solenoidal fields ≥ 24 Tesla prevent significant beam radius growth due to streaming.

Analytic estimates suggest other instabilities of the beam are less serious than the ion hose discussed above. Diocotron growth rates are too low to be significant, and filamentation should be controlled by the high fields and short propagation length required by the ion hose.

Three-dimensional particle-in-cell simulations were also carried out at LANL using ISIS-3D and IVORY to further investigate the onset of the ion-hose instability. Preliminary results show that the onset of ion hose instability depends on several parameters including the ratio of ion density to electron beam density, ratio of ion mass to electron mass, strength of magnetic field, waveguide wall radius, and ion emission area. Massive ions would decrease the growth rate, and a small density ratio (less than a few percent) would eventually stabilize the instability. Under certain conditions, the instability growth could also be suppressed by increasing the external magnetic field, or by reducing the outer wall radius. Experimental characterization of anode plasma would provide extremely useful information for understanding and controlling potential instabilities. The most important data would include ion density or current, ion species, and spatial distribution of the plasma. In addition, some analytic work and simplified simulations are needed to discriminate the different types of instabilities, analyze their growth rates, and evaluate proposed stabilization mechanisms.

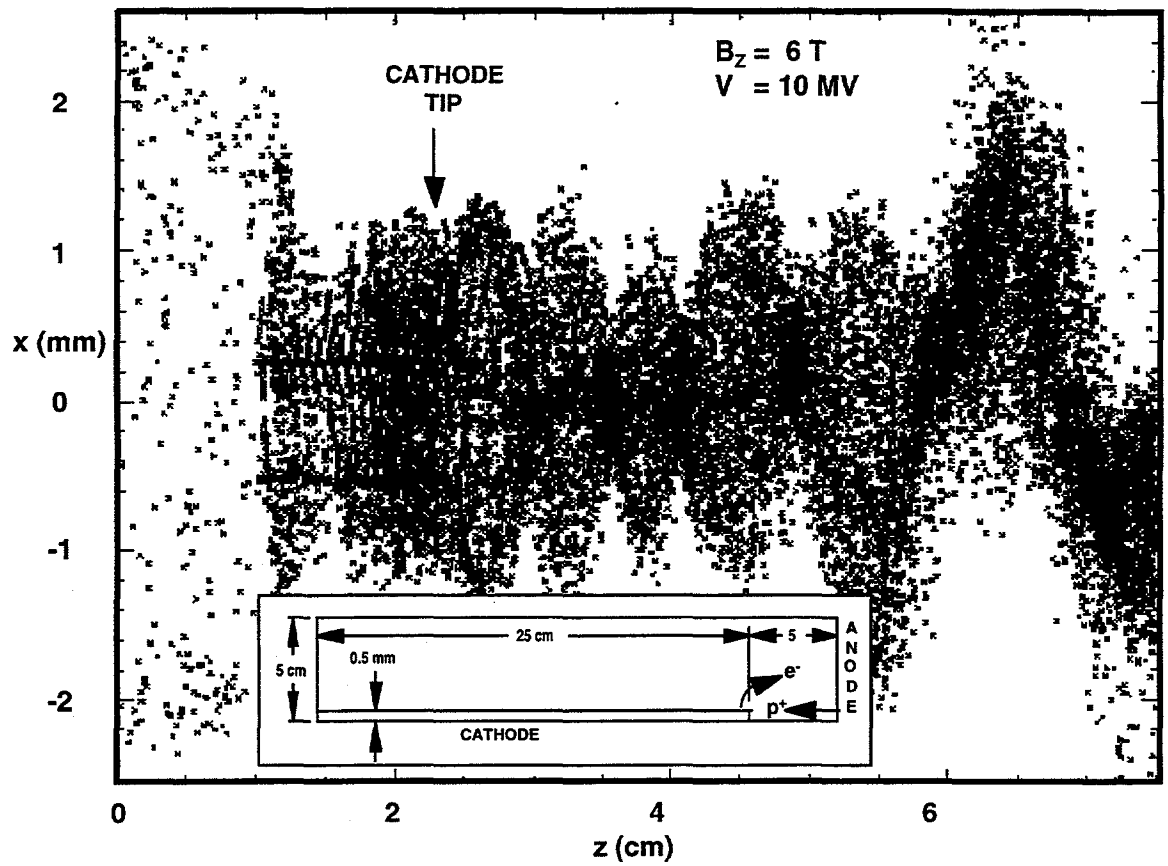

Figure 13. Top view of the electron distribution for an IVORY diode simulation including ion-hose effects. The insert shows the diode region included in the simulation.

VIII. 3D Beam Formation Asymmetry Calculations

The formation and expansion of a cathode plasma from the 0.05-cm cathode tip in SABRE could, under certain conditions, increase the emitted electron beam size. Such an increase is important as it could have adverse impact on image resolution needed for radiographic applications. An analytical estimate of macroscopic energy deposition in the SABRE cathode tip shows that Joule heating is not sufficient to form a plasma. Local processes such as explosive emission of electrons from the cathode surface are more likely plasma sources. Because of microscopic surface imperfections, the electric field enhancement will vary and consequently emission of electrons may be patchy along the cathode shank. The LANL 3D particle-in-cell code ISIS-3D was to simulate asymmetric emission of electrons and characterize the subsequent electron beam. Electrons were found to quickly acquire azimuthal E×B velocities after emission, which spread the space charge so effectively that the irregular emission had no impact on the electron beam distribution. Careful comparison with uniform-emission calculations revealed no change in the current, beam radius, or beam quality.

Since the cathode stalk is 8 meters long, there is a concern about its misalignment with respect to the axis of the coaxial line due to gravity and an effect on beam spot size. ISIS-3D was used to simulate the last 8 cm of the diode with an AK gap of 5 cm where the cathode tip was tilted 1.43 degree with respect to the axis. This misalignment is equivalent to a radial displacement of the cathode tip from the axis by one cathode radius over a longitudinal distance of 2 cm. The simulation shows that the electrons emitted from the shank follow along the cathode surface and are confined by the strong external magnetic field (24 T) after coming off the cathode tip, resulting in a final electron beam displaced by one radius in the transverse direction. The spot remains almost circular, and the beam radius is not significantly altered.

Finally, it is possible for the cathode plasma, under differing circumstances, to either diffuse across or deform the strong axial magnetic field, forming a larger cross section electron beam source. The ISIS results above suggest azimuthal source emission asymmetries are rapidly smoothed, so enhanced radial diffusion seems unlikely. The final calculations deal therefore with bounding the impact of bulk radial plasma motion. Cathode plasmas must be greater than the electron beam density (10^{15}/cc) to affect the resulting radiographic spot. Simple plasma β arguments suggest uniform 10^{15} cathode plasmas below 15 keV would be trapped by the applied 25-T axial field. Since this temperature exceeds any reasonable estimate of cathode plasma formation, beam-density-plasmas are believed to be well confined. The other end of the spectrum is low temperature solid density plasmas evolving off the cathode tip. LANL performed a series of 1D MHD calculations with assumed initial temperatures to characterize the outer edge of an expanding cathode plasma.[22] For high-conductivity tungsten plasmas, magnetic field diffusion is negligible for a 50-ns pulse width, and as the plasma distorts the applied field, the quality of the emitted beam may be affected. Depending on initial temperature distributions in the cathode tip, the effective cathode radius could increase substantially over times of interest for radiographic studies (Fig. 14). Recall that no known energy transfer mechanism is known to drive such plasmas, and experimental data are needed to establish a meaningful correlation between the calculations and the actual conditions in the cathode plasma. Limitations in the validity of the electrical conductivities from the SESAME tables are apparent below a few eV; additional conductivity models and data exist that may prove more accurate at lower temperatures, should the experiments indicate a need to study this regime.

IX. Target Hydrodynamic Response

A brief analysis was performed to examine the thermomechanical response of the target. ALEGRA,[23] a multi-material arbitrary Lagrangian-Eulerian shock wave physics code developed to simulate 1-, 2-, and 3-D time-dependent large-deformation dynamics was used.

A schematic of the calculation is presented in Fig. 15. All materials are modeled without material strength using SESAME equations of state: tantalum #3520; Teflon (instead of graphite) #7190; and titanium #2961. Since ALEGRA does not have an electron deposition capability, monte carlo estimates of the energy loss were directly deposited in

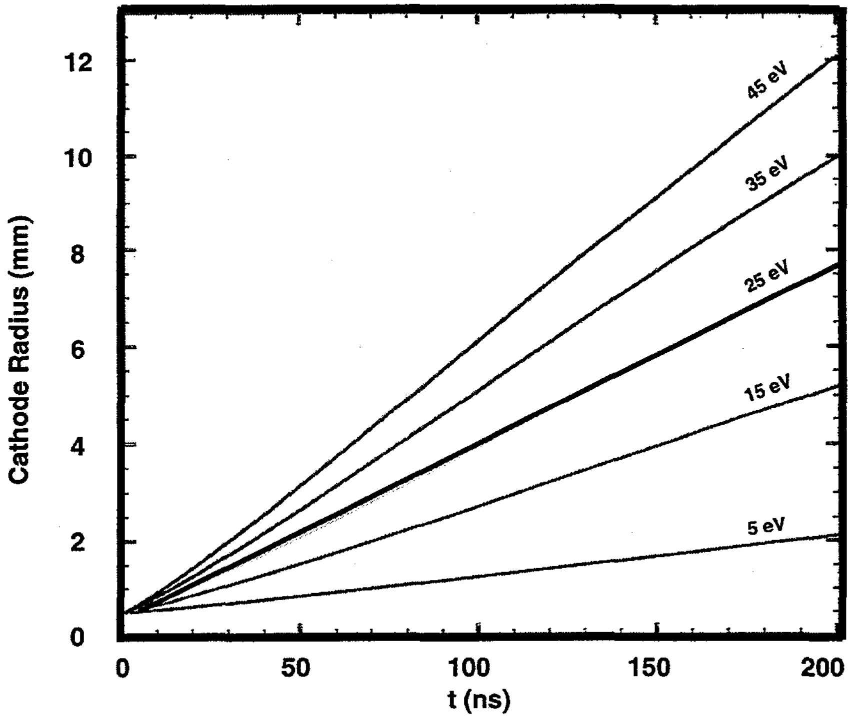

Figure 14. Outer cathode radius as a function of time, for an initial radius of 0.05 cm and for uniform initial temperatures of 5 eV, 15 eV, 25 eV, 35 eV, 45 eV in the tungsten cathode.

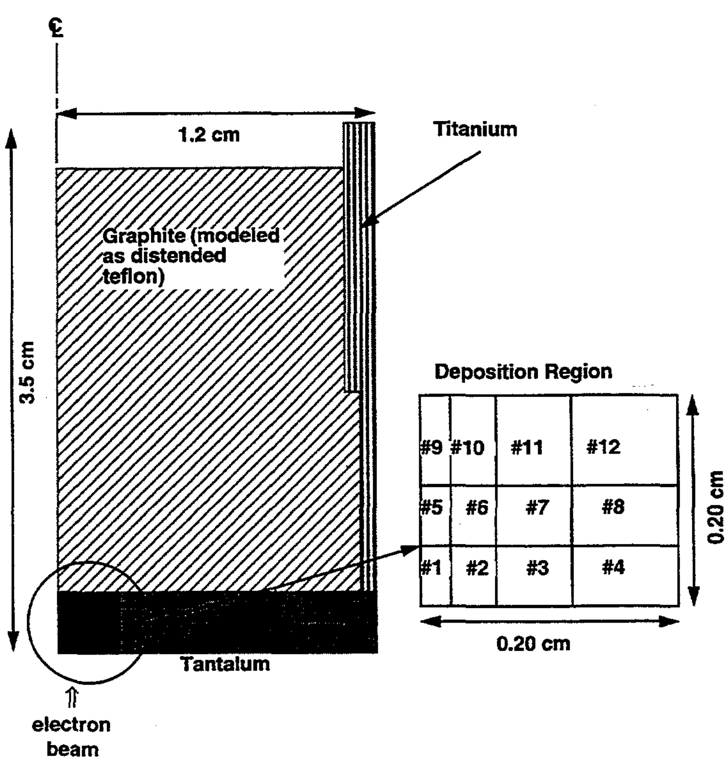

Figure 15. Schematic view of the calculated region of the bremsstrahlung target (not to scale) hydrodynamically modeled with ALEGRA.

twelve separate regions of the tantalum target (Fig. 15) with the temporal profile shown in Fig. 16.

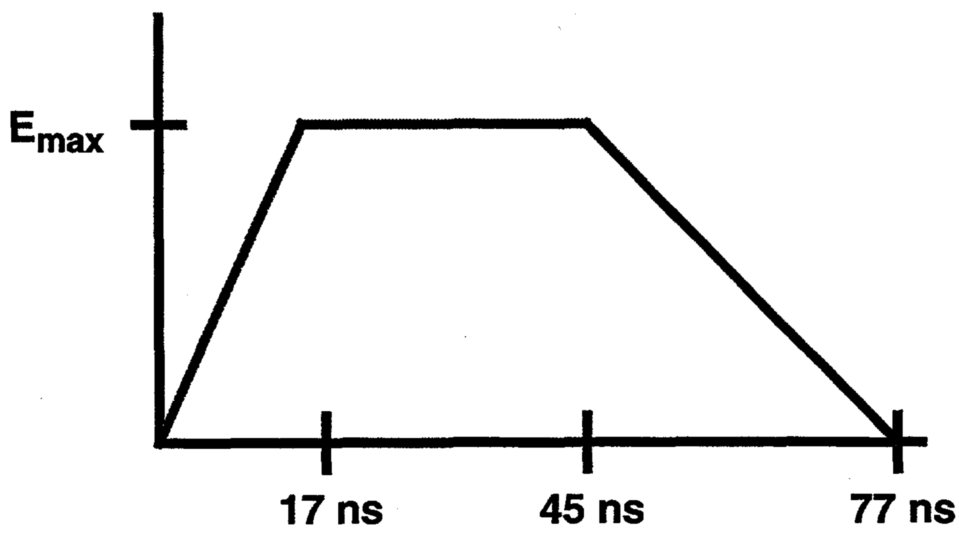

Figure 16. Temporal profile for the specific energy deposited in each of the twelve ALEGRA source regions.

The temporal behavior used in this calculation mimics more detailed static material electron deposition calculations where the 2D PIC electron distribution (Fig. 8) serves as input to monte carlo electron transport. In addition, from those more detailed calculations, the total fluence into each of our defined deposition regions can be derived. This determines the E_{max} parameter in Fig. 16. The resulting characteristics of each of the twelve deposition regions are summarized in Table 2. There the radial and axial extent of each region is given by the four parameters $\mathbf{r}_{min}$, $\mathbf{r}_{max}$, $\mathbf{z}_{min}$, and $\mathbf{z}_{max}$. The total deposited energy in the calculation based on this approximation is 1.5×10^{11} erg, which agrees favorably with the result of 1.6×10^{11} from the more detailed calculations.

Figure 17 shows the distorted computational grid 3 ns after the 77-ns electron pulse. While there has been some motion during the pulse, the overall volume change is about 15%. Thus, both the monte carlo treatment of electron energy deposition into static materials, as well as the apriori pure internal energy deposition in a series of self-consistently expanding region techniques, seem to be reasonable. The limited target motion during the drive pulse suggests minimal beam-plasma interaction volume, reducing the concerns of target motion affecting the x-ray source spot dimensions.

Table 2

Deposition region parameters by region

Region #	r_{min} (cm)	r_{max} (cm)	z_{min} (cm)	z_{max} (cm)	E_{max} (10^{20} ergs/cc)	Fluence (TW/cm^2)
1	0.0	0.02	0.0	0.06	3.7	2.2
2	0.02	0.06	0.0	0.06	8.0	2.2
3	0.06	0.12	0.0	0.06	0.7	0.4
4	0.12	0.20	0.0	0.06	0.2	0.1
5	0.0	0.02	0.06	0.12	6.5	3.9
6	0.02	0.06	0.06	0.12	5.8	3.5
7	0.06	0.12	0.06	0.12	1.8	1.1
8	0.12	0.20	0.06	0.12	0.3	0.2
9	0.0	0.02	0.12	0.20	2.7	1.6
10	0.02	0.06	0.12	0.20	2.3	1.4
11	0.06	0.12	0.12	0.20	1.3	0.8
12	0.12	0.20	0.12	0.20	0.3	0.2

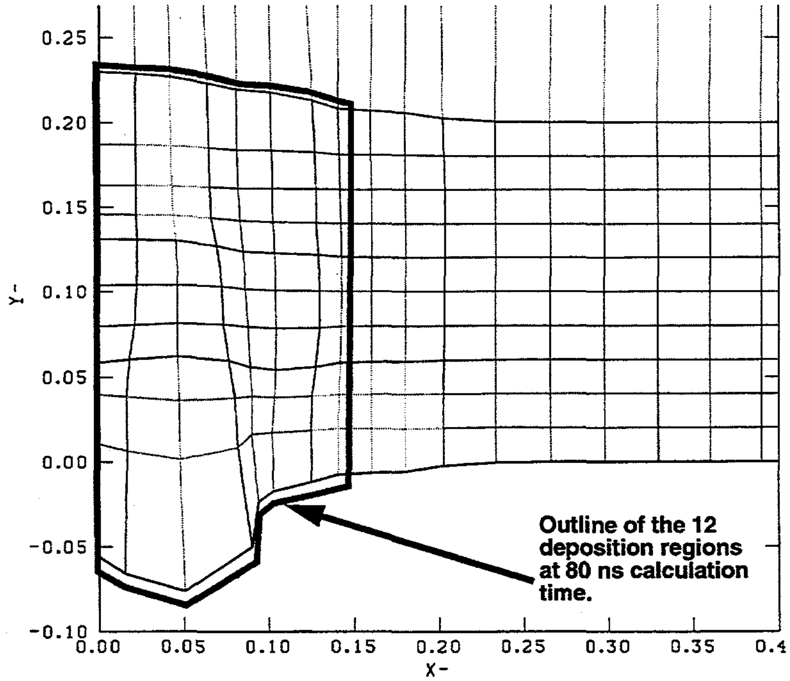

Figure 17. ALEGRA grid distortion at 80 ns, immediately following the drive pulse shown in Fig. 10. The deposition regions have expanded about 15% in volume.

The energy deposition due to electrons is quasi-volumetric since the material moves relatively little. This means that high peak pressures and temperatures will develop during the deposition. These will rapidly fall off during post-deposition expansion of this material. For the present calculations, peak equilibrium temperatures (near the end of the pulse at 77 ns) of 3 to 24 eV from the lowest to the highest fluence regions were observed. The residual temperatures in the deposition material 1.8 μsec later are still between 2 and 10 eV. This means that the material was vaporized by the deposited energy and should be expanding in a plume of vapor and partially ionized plasma as it is seen to do in the calculation. The expansion velocities lie between 0.5 and 4 cm/μsec, with the fastest velocities of greater than 1.5 cm/μsec being associated with the four deposition regions along the free surface: #1, #2, #3, and #4 moving principally normal to the surface.

Volumetric heating creates huge pressures between one and ten megabars depending on the region fluence, which fall rapidly as the material begins to expand. However, there is enough time to propagate high pressure into the "cold" tantalum and graphite not exposed to the electron. If the cold tantalum is placed under sufficient stress rapidly enough it will be damaged and will likely contribute to overall debris emanating from the target fixture. This calculation therefore studied the pressures delivered to the tantalum bordering the deposition region.

The rapid fall-off of deposition region pressures due to expansion rapidly attenuates the pressure pulse which propagates into the cold tantalum. Near the boundary of the deposition region, at a radius of 0.22 cm, the peak pressure in the tantalum is around 1.7 Mbar. At a radius of 0.37 cm, the peak pressure is near 500 kbars. These pressures are sufficient to deform the tantalum and create a crater larger than the electron beam size. To predict the ultimate crater radius, the cold tantalum must be further modeled with material strength, and the calculations must be run to substantially longer durations.

The pressure pulse in the cold tantalum is followed by a tensile region (due to radial divergence of the pulse) that would likely fracture the tantalum out to some radius, possibly creating additional debris. Thus, some tantalum surrounding the electron beam deposition region will be deformed, damaged, fragmented, and ejected by the forces created during the deposition. Based on experience with hypervelocity impact craters, the time scale for this ejection is much longer than the pulse width, and much of the ejecta will move at less than 1% of the speed of the vapor plume.

Graphite debris is also observed in the experiment, so the calculation further addressed the nature of the wave propagation into the graphite. The graphite was modeled as Teflon which will attenuate shocks more slowly than a true porous material. Thus, the present calculations should provide an upper bound on the strength of the pressure wave in the graphite as a function of time. The wave attenuates from: hydrodynamic attenuation (the rarefaction which follows the shock wave moves faster than the shock), divergence (it is almost spherical divergence in the present case because the source region is relatively small compared to the overall fixture), and energy dissipation in the graphite. The calculations did not run long enough to gauge the true extent of the pressure wave damage in the graphite.

The Lagrangian grid in the deposition region ultimately distorted and stopped the code at 1.8 μsec. A portion of the computational grid at 1.0 μsec is illustrated in Fig. 18. At the location A, the pressure wave has attenuated to about 50 kbars. The wave attenuates more slowly near the axis of symmetry so a corresponding isobar location is further into the graphite bulk. However, even with a relatively poor material model for graphite, the indications of the present calculation are that a damaging pressure wave would not arrive at the titanium case surrounding the bremsstrahlung target.

This calculation would be improved by using a porous model for the graphite, even if the solid matrix was not strictly modeled as carbon. This is currently possible in one model in ALEGRA. In addition, material strength should be added to the tantalum to more accurately arrest the growth of the crater. The calculation would also be improved if we utilized the ALEGRA capability to model the deposition region as Eulerian while leaving the graphite and most of the tantalum regions as Lagrangian. This would prevent the mesh from tangling as the plume expands and allow longer duration calculations. Finally, the overall fidelity of the calculation would increase by using a finer computational grid.

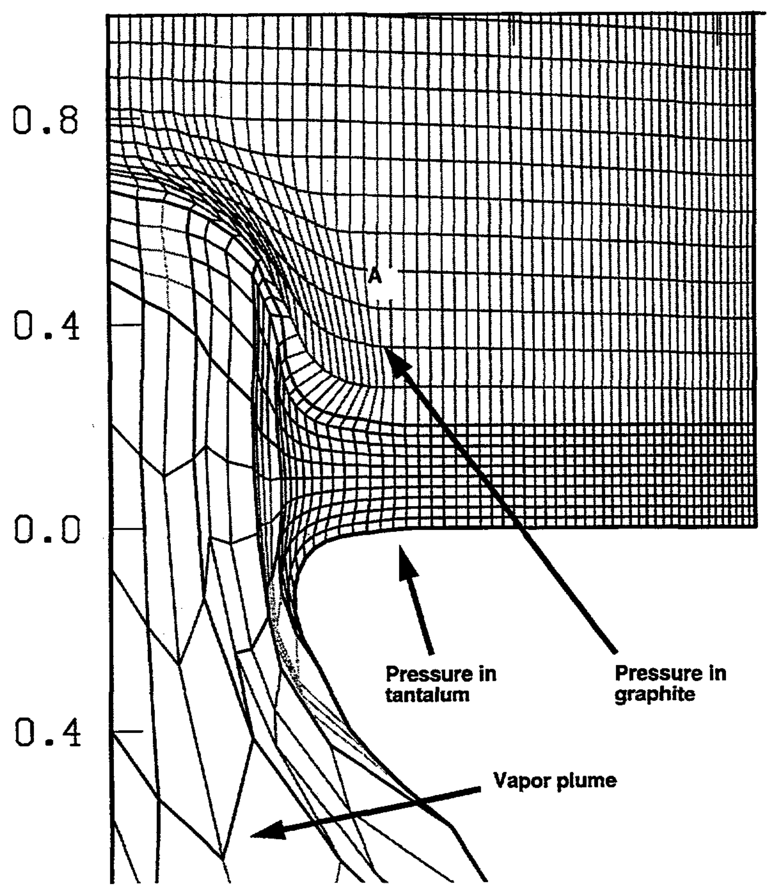

Figure 18. Deformed ALEGRA grid near 1.0 μsec. The deformation illustrates the formation and expansion of a vapor/plasma plume and the propagation of a pressure pulse into the bremsstrahlung converter. The location "A" is mentioned in the text.

X. SABRE Accelerator and Diode Performance

The SABRE accelerator performance was disappointing, due principally to the significantly different demands of this experiment compared to the usual positive polarity lower (4-5 MV) voltage operation.

The modifications discussed in Section II provided SABRE the means to exceed the 12 MV design envelope voltage. The Lucite insulating rings sustained damage approaching 10 MV. This situation was further aggravated by target debris from the initial design propagating upstream into the voltage adder contaminating the dielectric surfaces. A new target assembly, with the Ta bremsstrahlung converter encapsulated inside a stainless steel shell and backfilled with graphite, reduced the target debris to minimal (~ gm) levels of vaporized material and eliminated this problem.

An extended period of inability to synchronize the two electrically triggered transfer gas switches at the new operating point further delayed the experiment. The problem was solved by installing more reliable Saturn[24] switches.

Voltage prepulse was found to severely affect the diode performance. Ground plates installed near the peaking switches[9] reduced the water transmission line capacitive coupling and reduced the prepulse amplitude by 50%. This step also reduced the power pulse FWHM by 10 ns. An additional MITL flashover switch succeeded in eliminating the prepulse problem.

The modifications in Section II, along with those discussed above, narrowed the SABRE trapezoidal output voltage pulse to triangular with only 30 ns FWHM. This, together with the lower peak operating voltage imposed by the insulator rings, limited the maximum x-ray dose to 20% of the anticipated krad levels. Approximately 20 good shots in this final experimental configuration are discussed below.

The magnetically immersed foilless diode hardware (Fig. 19), including the titanium housing, cantilevered cathode electrode, tungsten needle, target holder, current diagnostics, and 20-T magnet solenoid, met and even exceeded design specifications. Two 30-Tesla coils were built; one using the 20-Tesla coil wire and design, and the other using a new, stronger Be-Cu wire. The latter failed after a few shots, but the standard wire coil operated at 30 Tesla flawlessly. There was no downtime due to diode problems. The specially designed 2-MJ radiographic capacitor banks were delivered too late to be used in this experiment, and the borrowed banks which were used experienced a number of difficulties.

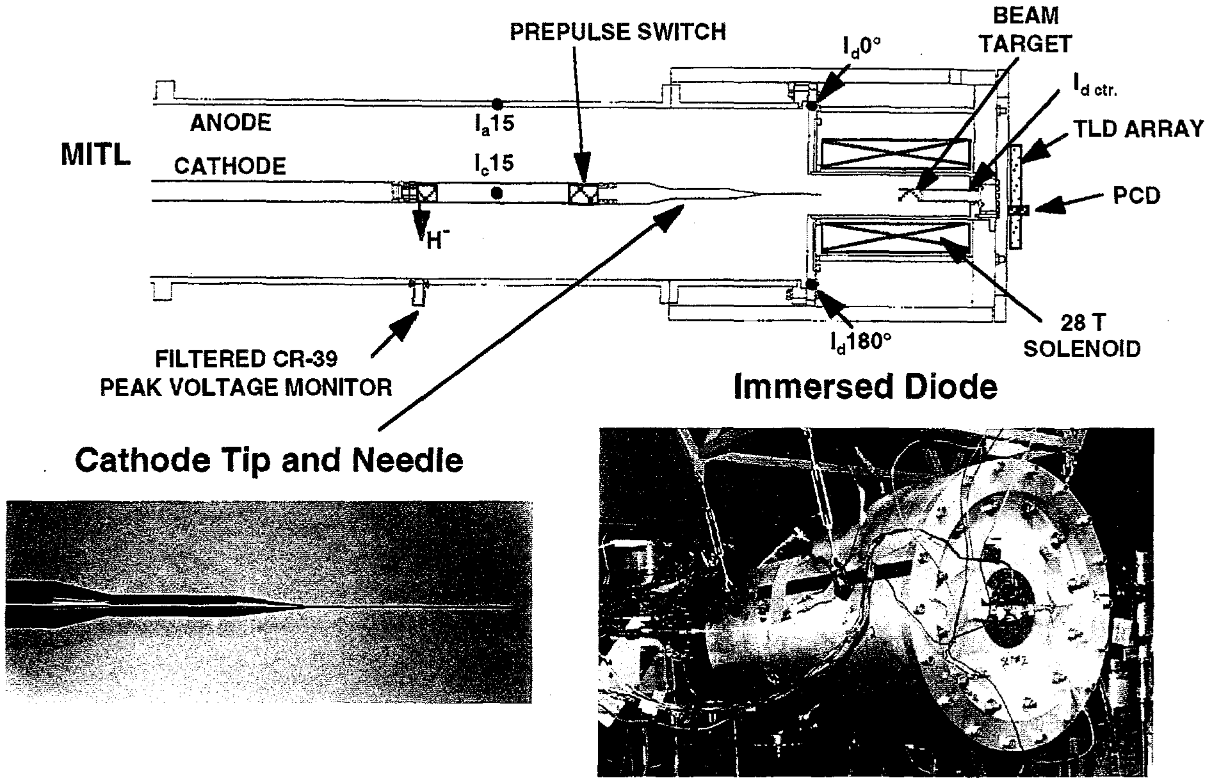

Figure 19. SABRE extension MITL and immersed-diode assembly. The location of many diagnostics is also indicated.

XI. Diagnostics and Experimental Results

The current pulse propagating through the voltage adder and extension MITL was measured with $\partial B/\partial t$ ($\dot{B}$) diagnostics located on the outer anode electrode (A1 - A15) and on the inner cathode electrode (C4 - C15). The number corresponds to the detector axial position (in meters from the low voltage end of the accelerator). The monitors A15 and C15 were ~ 1 m before the diode (Fig. 19) and were used to infer the voltage pulse using Creedon's steady-state parapotential flow theory.[11] The peak voltage was corroborated with the kinetic energy of H^- ions born on the cathode and radially accelerated to the anode near location 15. This technique uses an array of ion range filters to identify the highest kinetic energy band to record on a CR-39 film substrate. As discussed later, these measurements are in good agreement with the parapotential flow voltage calculations.

The beam current was measured with 5 $\dot{B}$s monitors. Four were azimuthally spaced about the entrance of the diode anode cylinder [$I_d0°$, $I_d90°$, $I_d180°$, $I_d270°$] (Fig. 19) and the fifth [$I_{d\,ctr}$] was near the base of the target holder. These five $\dot{B}$s were externally calibrated to ~ 15%. The other $\dot{B}$s were calibrated *in situ*, using a current pulser in combination with a precision resistor, to an estimated accuracy of ~ 20%.

The bremsstrahlung temporal evolution was monitored with a diamond photoconductive detector (PCD)[25] located near the axis 22 cm beyond the target (Fig. 19). These detectors were developed in an earlier Sandia-Los Alamos collaboration and were provided by Los Alamos for these experiments. The time-integrated x-ray radial profile in the same plane was measured with two orthogonal arrays of 15 CaF_2:Mn thermoluminescent dosimeters (TLD) equally spaced at 9-mm intervals. The 30-Tesla solenoid was shorter (1/2 length) than the baseline 20-T configuration, requiring a longer target holder. Hence, for the higher field shots, the TLD plane was located 30 cm from the target. The polar x-ray dose distribution is insensitive to the beam spot size but provides information which, when used together with radiation transport monte carlo simulations (CYLTRAN[26]), estimate the electron beam temperature.

The electron beam profile evolution at the target was inferred from its bremsstrahlung signature, measured with a fast-framing x-ray camera (Fig. 20). This camera was developed at Sandia National Laboratories for the HERMES-III and RADLAC-II experiments.[27] The x-ray source was imaged through eight 0.7-mm (min) diameter long tapered pinholes in separate lines of sight onto discrete sealed microchannel plate detectors which were pulse biased to provide sequential 6-ns frames during the SABRE power pulse. In addition, two lines of sight recorded time-integrated images. Numerical simulations with CYLTRAN suggest that, for the thin Ta targets with graphite backing, the electron beam size equals the measured x-ray spot size.

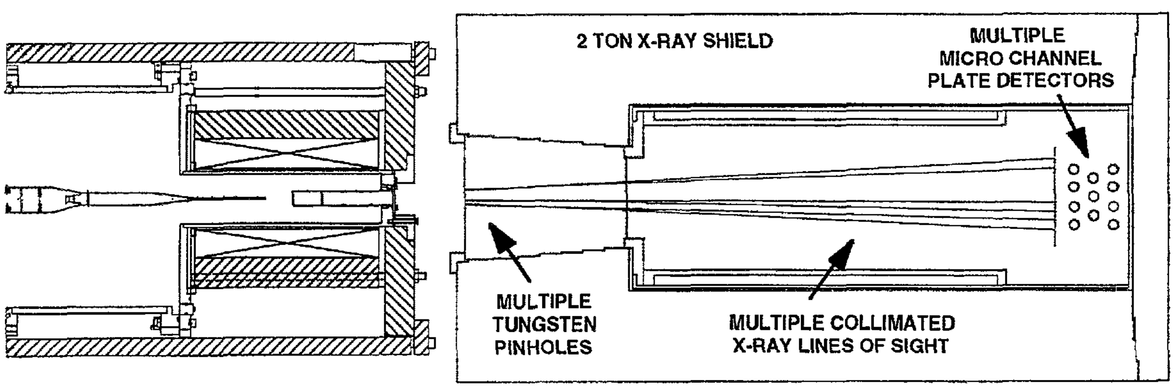

Figure 20. Multiframe time-resolved x-ray pinhole camera geometry, providing two time-integrated and five time-resolved (6-ns wide) frames.

The time-integrated x-ray source size was also measured with the AWE technique.[28] A 5-cm thick 1-m radius tungsten edge and a lead shielded shadowgraph box camera was built to AWE specifications. Dave Forester and Ray Edwards of AWE fielded the apparatus, corroborating the fast-framing camera data. For a number of shots, the x-ray source size and dose were also measured with the circular edge LANL technique by Scott Watson and his team.[29] Their measurements confirm the SNL and AWE source size and dose measurements.

On one shot (#1575), a fresh titanium needle holder was used and subsequently analyzed for the induced activation spectra[30] to estimate the mean energy and charge of backstreaming protons. A number of activation products were found, including V-47 and V-48 which are the result of (p,n) reactions on Ti. The ratio of V-47 to V-48 activity can be used to estimate the mean proton kinetic energy (see Fig. 21). The ratio of activities measured on SABRE corresponds to protons just over 7 MeV. This is a weighted average but is skewed high because the cross sections are increasing dramatically in this range. Assuming <7 MeV> and a 90% pure Ti target, there were 3.5 J of protons, corresponding to an average proton current of 5 A. This lowest boundary value is well within the ion current envelope predicted by the PIC simulations and is, therefore, consistent with our understanding of the immersed diode behavior.

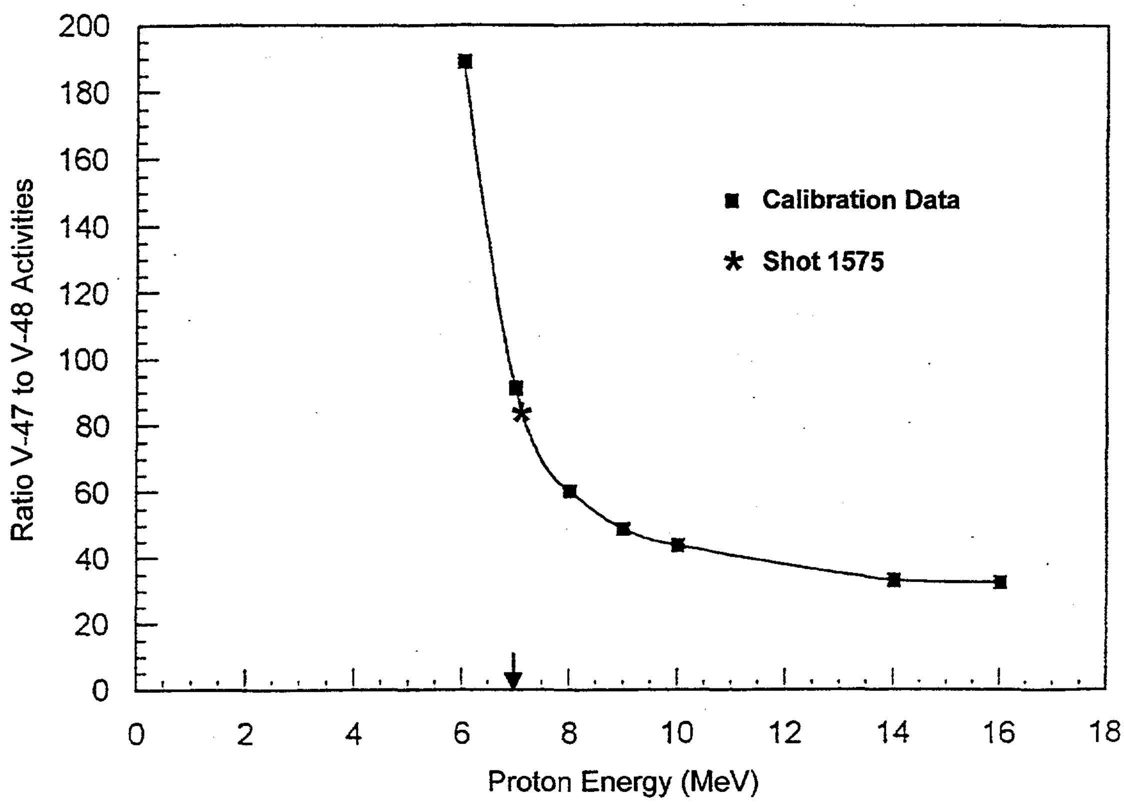

Figure 21. Ratio of V-47 to V-48 activity versus proton energy.

The baseline diode configuration described in Sections IV and V exhibited two serious difficulties: a severe decrease in the diode impedance near the peak of the voltage pulse and a larger-than-predicted beam size. Both were successfully resolved.

A. Current Measurements

Figure 22a shows the anode (total) currents entering the voltage adder (A1) and exiting the 3-meter extension MITL (A15). The differences are within the calibration accuracy of ~ 15%: it is clear that current transport is very efficient. The cantilevered MITL cathode electrode was instrumented after cavities 4, 7, 8, and at 15 meters (Figure 22b). The difference between anode and cathode current is the electron sheath current at each location (Fig. 22c). The MITL currents scale with the peak output voltage are in good agreement with TWOQUICK simulation (Fig. 6).

Diode beam currents are shown in Fig. 22d. All five monitors agree within the calibration accuracy. The measured beam current amplitude is also in good agreement with simulation predictions. The difference between the MITL anode (total) current (Fig. 22a) and the diode (beam) current (Fig. 22d) is the sheath current diverted to the anode at the fringe field region as predicted by the numerical simulation (Fig. 6). This was confirmed with TLD and PCD measurements at the fringe field location.

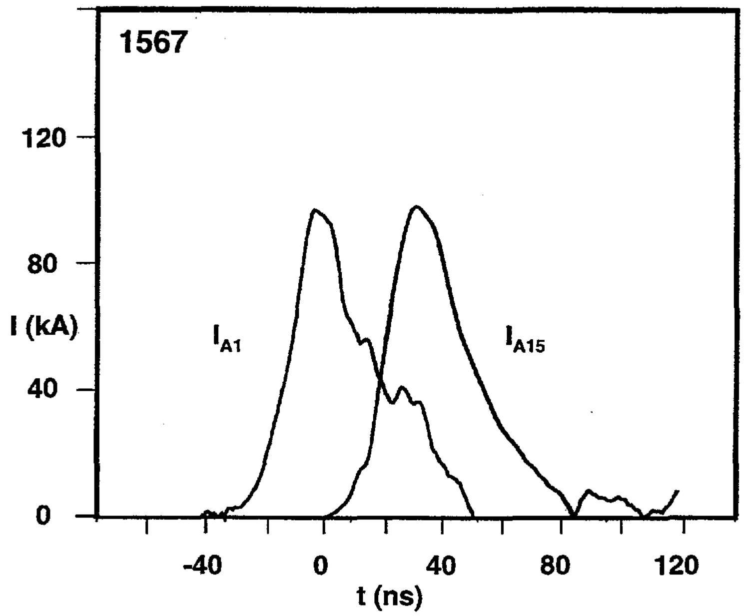

Figure 22. (a) MITL anode (total) currents for Shot 1567.

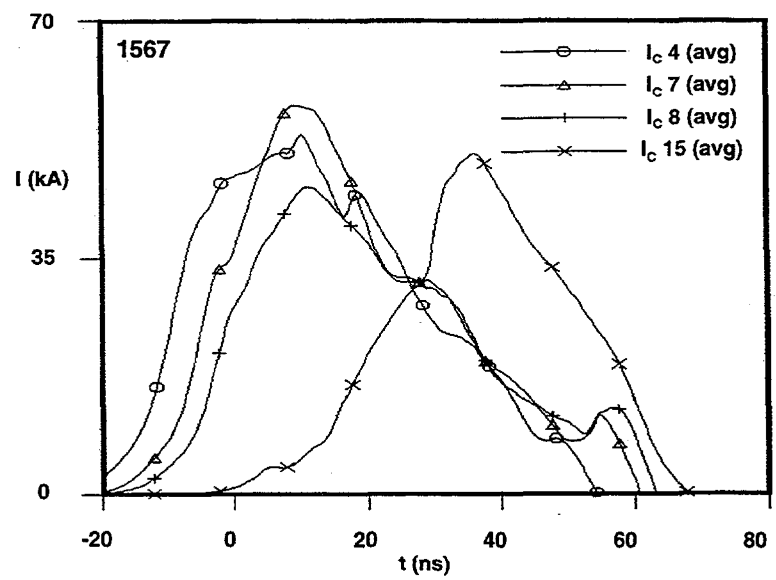

Figure 22. (b) MITL cathode (boundary) currents.

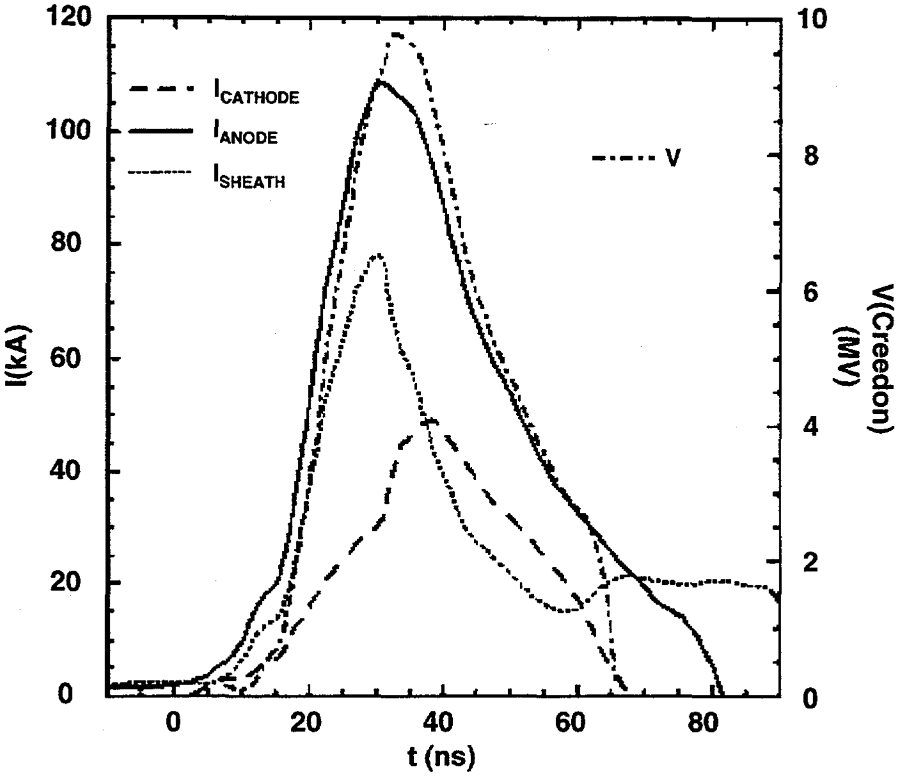

Figure 22. (c) 15-meter I_{Anode}, $I_{Cathode}$, I_{sheath}, V.

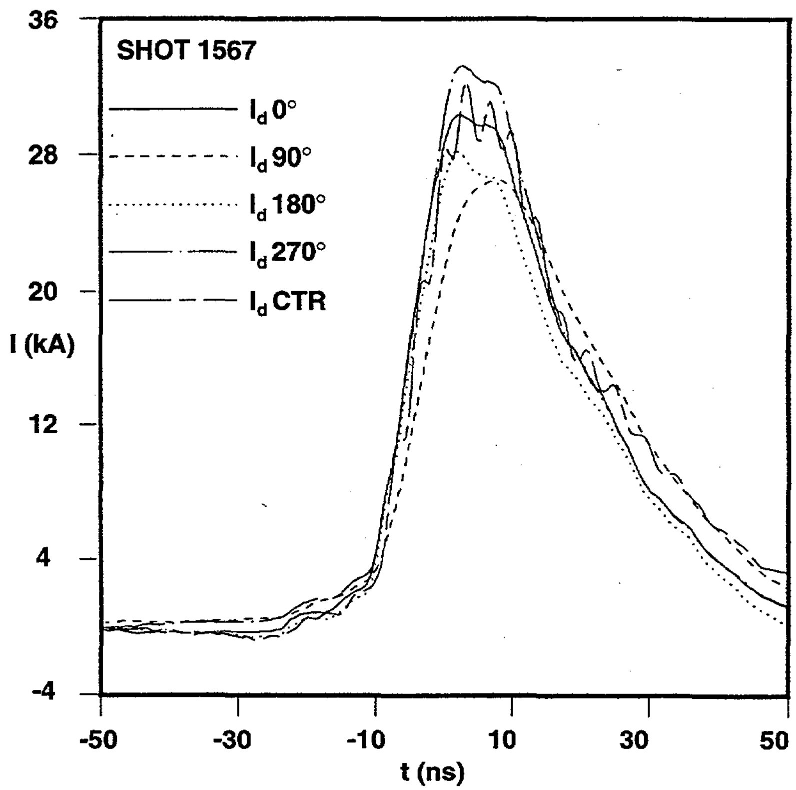

Figure 22. (d) Diode currents.

B. Voltage Measurements

The Creedon parapotential flow formalism uses A15 and C15 (Fig. 22c) to calculate the voltage profile and peak (V_c). This indirect measurement is corroborated by a direct ion range measurement of the peak voltage. Table 3 summarizes and compares both techniques for a number of shots.

Table 3

Shot No.	V_c (MV)	V CR-39 (MV)	I_b (kA)	PCD FWHM (ns)	f(t) FWHM (ns)	$(\beta_\perp)$*
1562	9.0	8.2 - 8.7	35	12.5	13.3	0.25
1564	8.8	8.3 - 8.7	32	13.2	12.8	0.11
1565	8.8	8.2 - 8.9	41	15.7	16.9	0.25
1567	9.5	9.2 - 9.7	29	12.6	13.2	0.21
1569	9.2	8.7 - 9.2	32	12.7	13.1	0.11
1575	9.0	8.7 - 9.2	30	14.6	14.9	0.22

*This is the $\beta_\perp$ utilized in Eq. (3) below to calculate the x-ray temporal evolution [f(t)].

C. Prepulse

The impedance decay was found to be correlated with the combination of poor vacuum (> 10^{-5} torr) and a ~ 100-kV prepulse arriving 200 ns before the main pulse. Because of the large field enhancement at the cathode needle, at high pressure the prepulse apparently produced enough plasma to affect diode operation 200 ns later when the main voltage pulse arrived. Figure 23 shows the 10-kV prepulse in one of the transmission lines. The voltage adder sums the 10 cavities to apply an estimated 100-kV prepulse to the diode AK gap.

A prepulse flashover switch together with the pulse forming line isolation plates solved this problem. The flashover switch was a 3-cm long dielectric section inserted before the transition region (Fig. 19), which calculations suggest should isolate the cathode needle from the prepulse while providing a low-inductance high-conductivity connection for the main pulse. A longer (more conservative design) switch could not be implemented without major hardware modifications. This switch was found to be effective when the load region pressure was less than 5×10^{-6} torr.

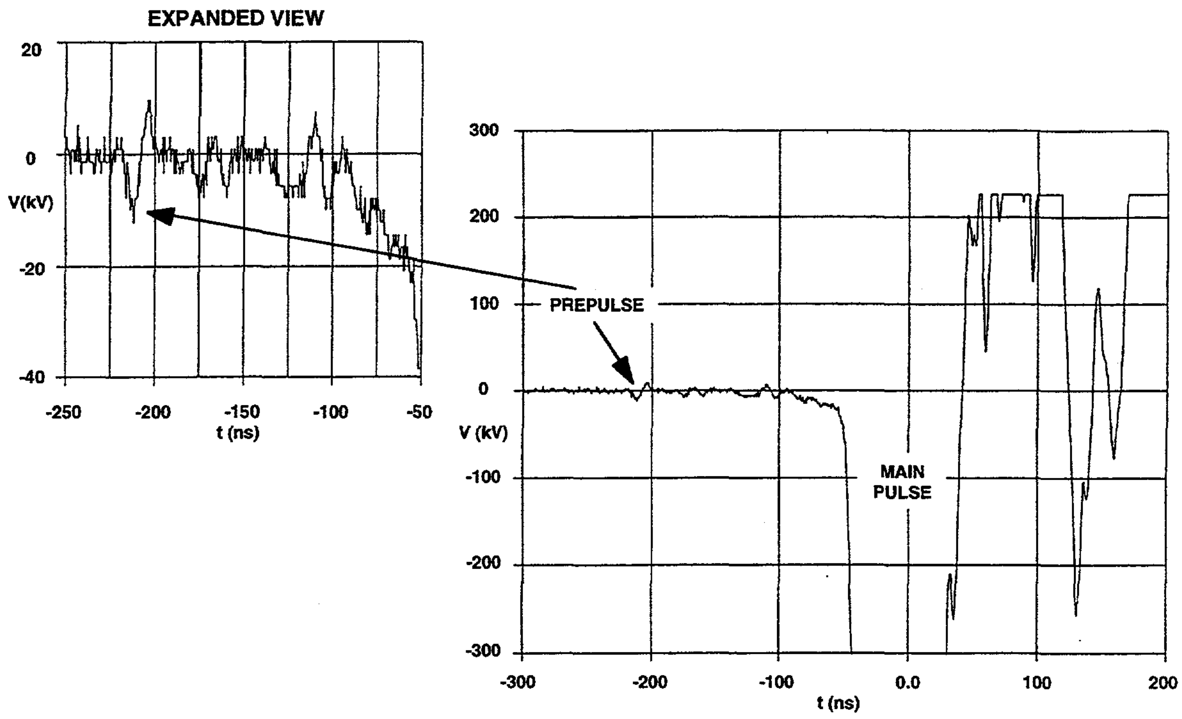

Figure 23. Prepulse measured in the output transmission line. The main pulse amplitude has been truncated to fit in the figure.

Figure 24 shows the anode and cathode currents at location 15 and the mean load current (a) without and (b) with the prepulse suppression switch. For similar drive pulses, the cathode current without the prepulse switch increases as the diode impedance decays. Figure 25 shows the voltage, diode current, and the predicted stable impedance profile for the latter shot. Without the prepulse switch, a similar figure cannot be constructed since when the impedance decays the cathode current no longer follows parapotential flow theory, and there is no method for inferring the voltage profile from the current measurements.

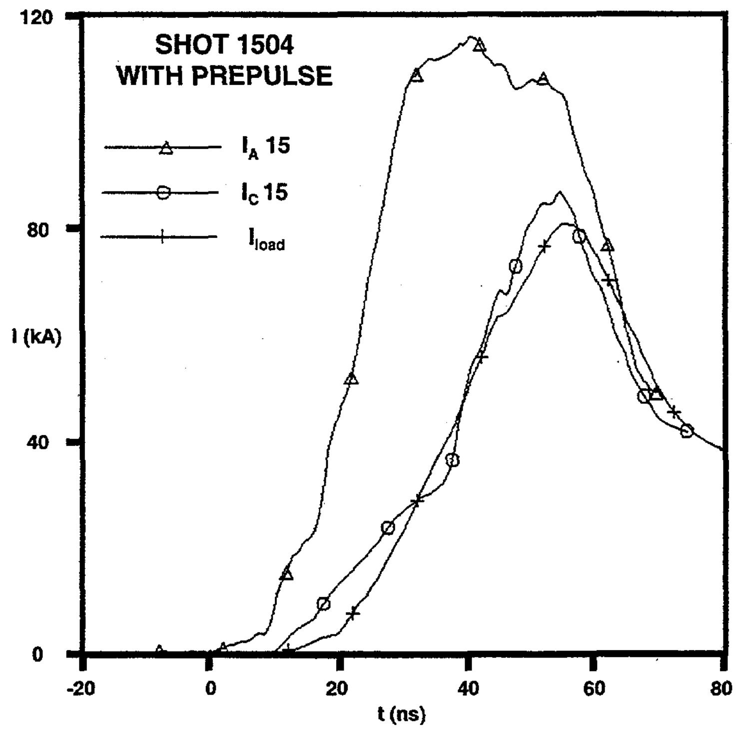

Figure 24. (a) Total (A15) and cathode boundary (C15) currents at location 15 and average load currents for shot 1504 without prepulse suppression. The cathode current becomes large (~ 100 kA) as the diode impedance decays.

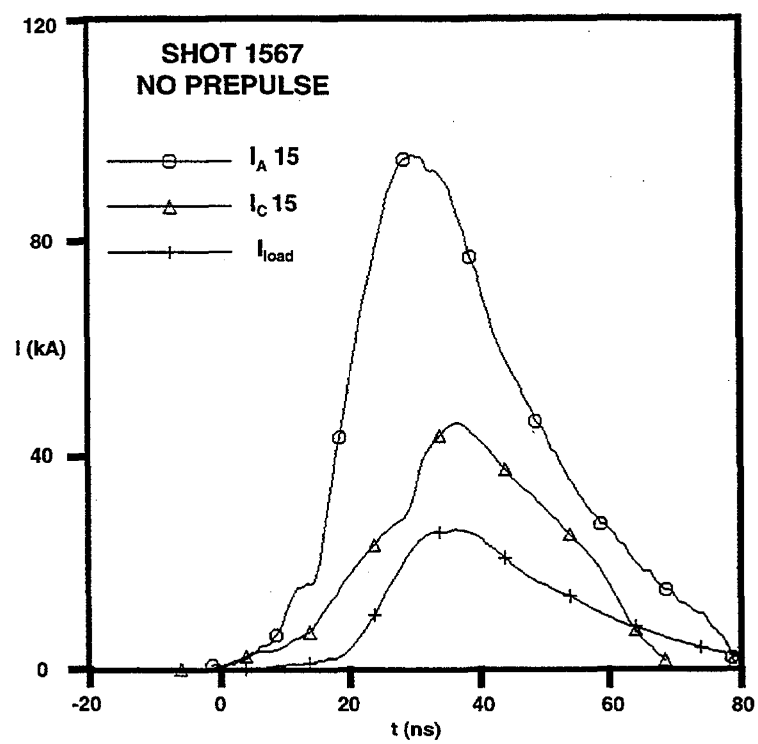

Figure 24. (b) Use of a prepulse suppression switch (Shot 1567) enables normal diode impedance behavior: the cathode current is ~ 40 kA.

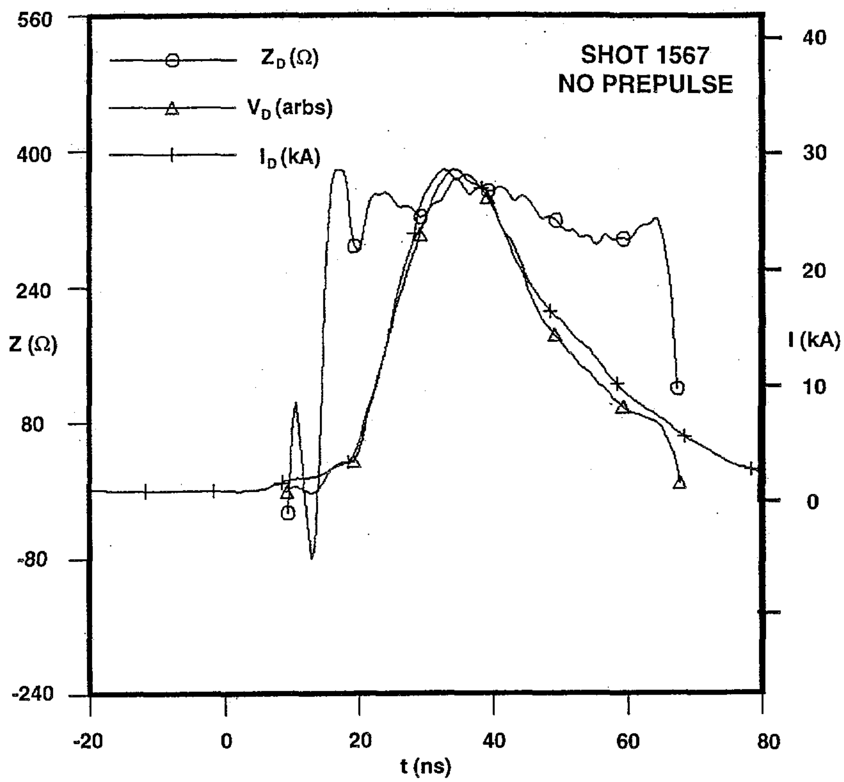

Figure 25. With prepulse suppression, the diode current I_d closely follows the diode voltage V_d, resulting in the anticipated and desired flat diode impedance profile.

D. Beam Transverse Velocity ($b_\wedge$) and Dose Measurements

The beam transverse velocity or temperature was evaluated by comparing the measured TLD polar radiation patterns with monte carlo radiation transport code (CYLTRAN[26]) predictions using the actual hardware geometry and x-ray converter target. Figure 26 compares the measured radiation profile with that expected assuming different beam temperatures ($\beta_\perp$): zero, 0.1 and 0.2. The data appears to match $\beta_\perp \sim 0.1$, about twice the predicted value without ions (Fig. 8) but less than simulations which include proton emission from the anode target (Fig. 10).

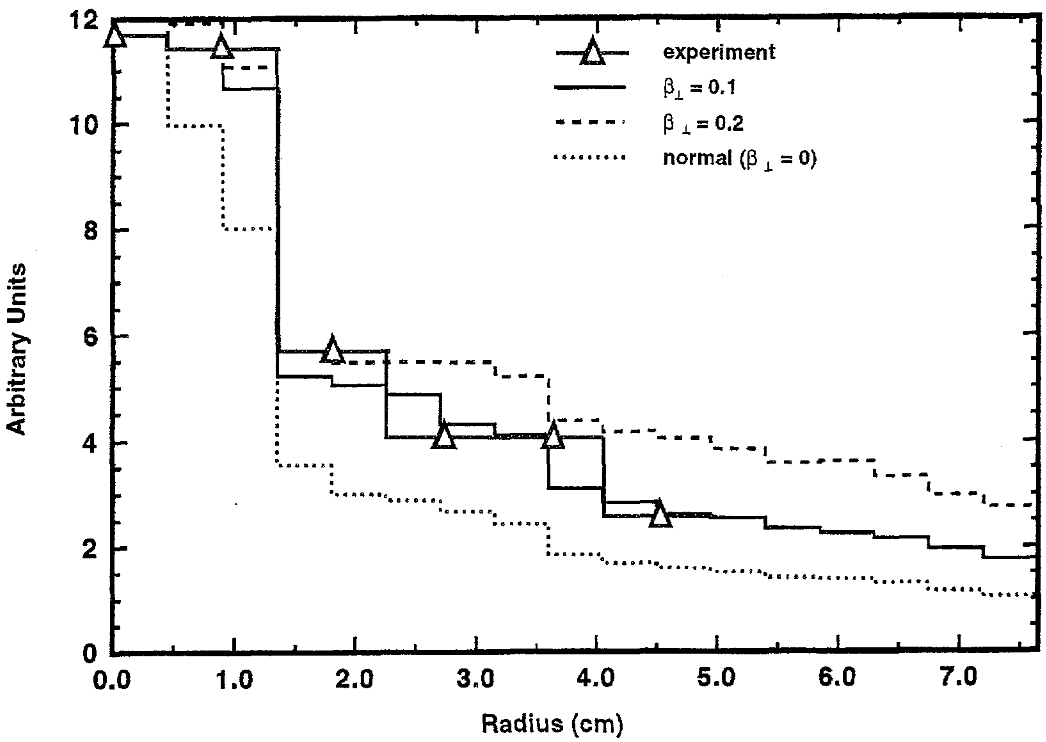

Figure 26. The measured radiation dose profile (triangles) is compared with the profile expected assuming three different beam transverse velocities $(\beta_\perp)$: 0, 0.1 and 0.2.

The beam temperature ($\beta_\perp$) significantly influences the on-axis dose. A semi-empirical expression of the bremsstrahlung x-ray production is[31]

$$f(t) = V(t)^{2.8} e^{-\frac{(V(t)+0.5)\beta_\perp}{.667\pi}} I(t) \tag{3}$$

where V is the beam voltage (MV), I is the beam current (A), and $\beta_\perp$ is the beam transverse relativistic velocity. The total dose on axis one meter from the source is $D = 1290\int f(t)dt$ (Roentgens).

Equation (3) and TLD dose measurements on axis were utilized to corroborate the time average beam temperatures shown in Table 3 (see Table 4). While the two methods yield comparable transverse velocities, the two TLD dose measurements on-axis technique cannot be as accurate as the 30-TLD polar diagram method (CYLTRAN comparison technique).

As a further consistency check, Fig. 27 compares the diode voltage, current, f(t), and PCD trace for Shot #1567. The PCD agrees very well with the calculated x-ray profile utilizing the measured voltage and current waveforms for a variety of shots (Table III). The time-integrated PCD waveforms are also in good agreement with the adjacent TLD monitor measurements.

Table 4

Shot No.	TLD Dose @ 1 m (R)	Transverse velocity ($\beta_\perp$) from comparison of TLD dose with calculated dose Eq. (3)	Transverse velocity ($\beta_\perp$) deduced from comparison of TLD dose with CYLTRAN simulations (Fig. 25)
1562	97	0.25	
1564	154	0.11	
1565	101	0.25	$0.1 < \beta_\perp \leq 0.2$
1567	128	0.21	
1569	204	0.11	
1575	114	0.22	

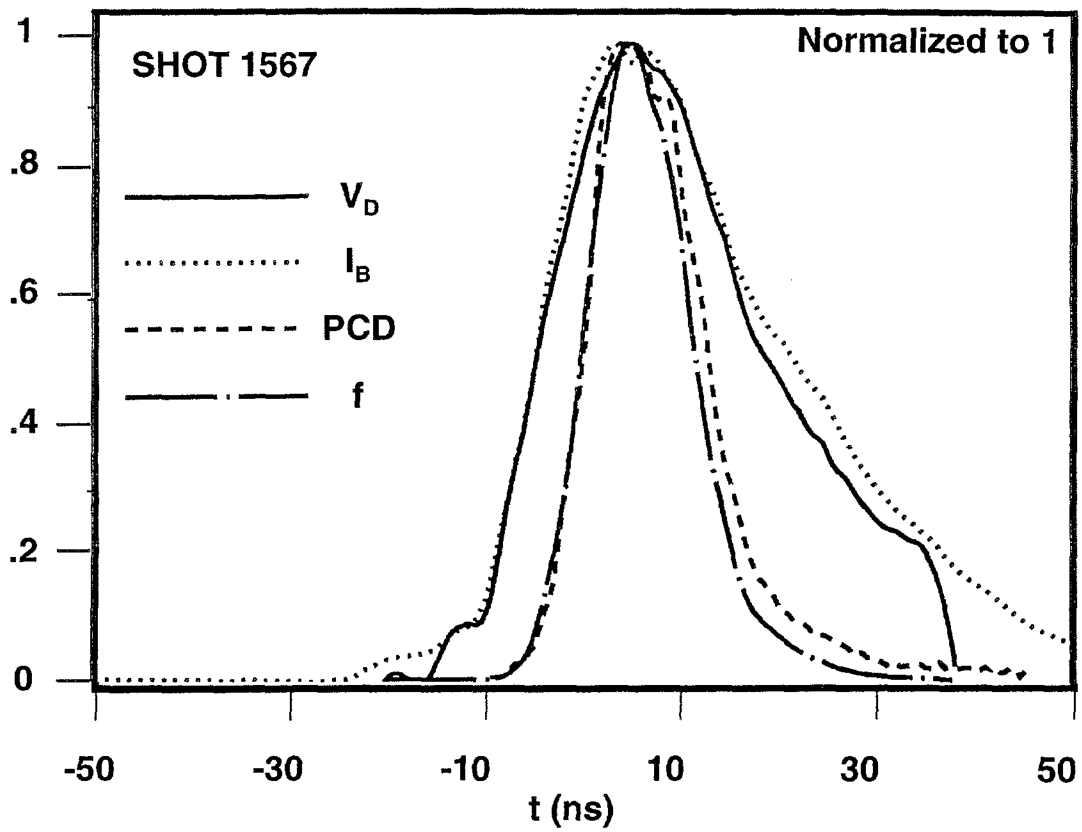

Figure 27. The diode voltage, current, x-ray pulse, and f(t) are shown (Shot #1567). The SABRE triangular power pulse produces an x-ray pulse much narrower than the voltage and current pulse (see Eq. 3).

The measured dose on axis extrapolated to 1 m from the target is on average 15% of that expected assuming a 40-ns FWHM trapezoidal power pulse, 12-MV diode voltage, 35-kA beam current, and beam temperature of 0.15 (Eq. 3). However, the SABRE pulse was triangular ~ 30 ns FWHM, the operating diode voltage between 8-9 MV, and the temperature ~ 0.15. These beam parameters explain the observed axial doses (Table 4). This analysis shows that a radiographic accelerator with a 12-MV, 50-ns square pulse, and 40-kA current would exceed of 1 kR at 1 meter, even with $\beta_\perp$ of 0.15.

E. Beam Spot Size

The multiframe time-resolved x-ray pinhole camera shown in Fig. 20 was used to evaluate the radiation source evolution produced by the high-intensity electron beam striking the grounded target. This information was essential to understand the beam dynamics and behavior. Figure 28 displays four sequential frames (timing shown in the insert) and a static time-integrating image of the x-ray production region for a low-field (6-T), 5-cm AK shot with a graphite target (#1427) and large prepulse. The beam moves from frame to frame, eventually breaking into clusters which spread beyond the line of sight. This data suggested an ion-electron streaming instability wherein ions emitted from the target (1.4 kA) interfere with the electron beam and cause it to oscillate.

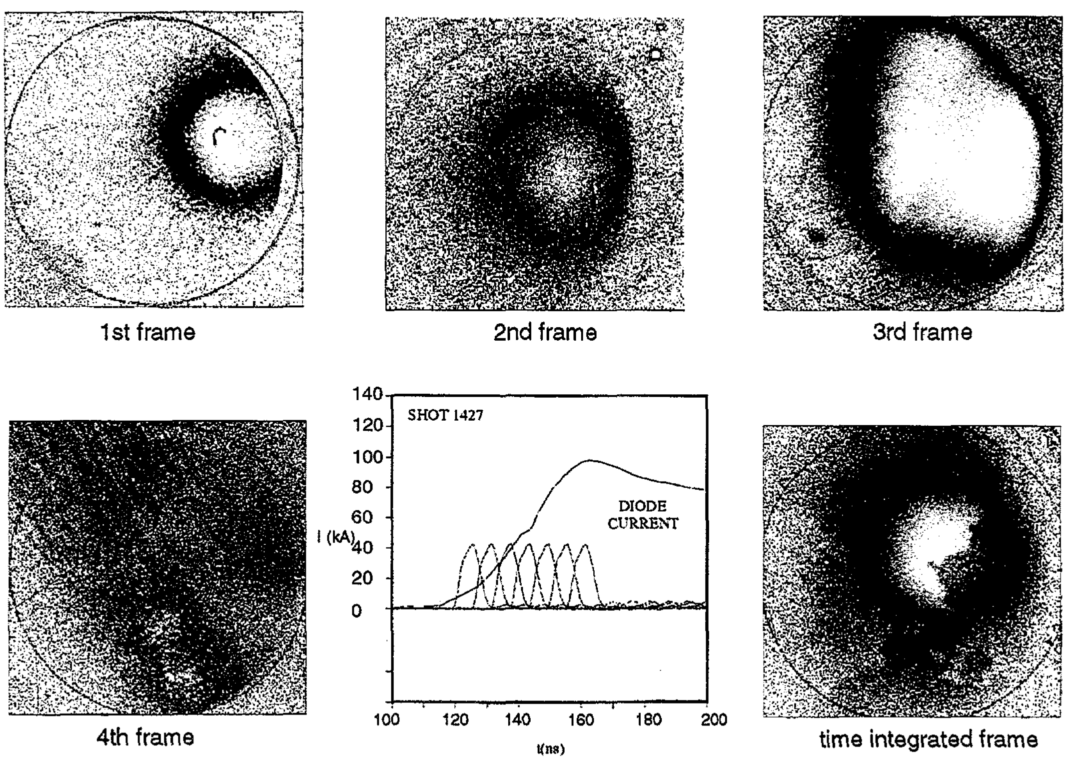

Figure 28. X-ray source evolution for a low (6 T) magnetic field, shot 1427. The beam grows and breaks into filaments by the third frame. Prepulse-induced impedance collapse limited the electron beam to only 24 ns (4 frames). The seven x-ray framing camera bias pulse timing versus the diode voltage is also shown (insert). Images are uncorrected film density.

Theoretical analysis and IVORY simulations suggest the ion-hose instability should saturate when the beam equals an electron Larmor radius. A preliminary analysis of shots varying the magnetic field confirms this scaling with the beam size decreasing inversely as the magnetic field intensity increases: the raw x-ray spot is ~ 3.5-4 mm at 15-20 Tesla and 2-3 mm at 26-29 Tesla.

Figure 29 shows the x-ray source evolution at high (29 T) magnetic field with the improved reduced-prepulse configuration in six frames (timing shown in the insert) and two static time-integrated images. These images were produced by scanning the films into specular density. An example of the detailed image analysis is given for the first time-integrated image in Fig. 29 (center frame on right). An x-ray flashlamp calibration was used to convert film density to exposure (ergs/cm^2) (Fig. 30), which was used to unfold the image (Fig. 31). The system magnification has been corrected so the lineouts are in x-ray source dimensions.

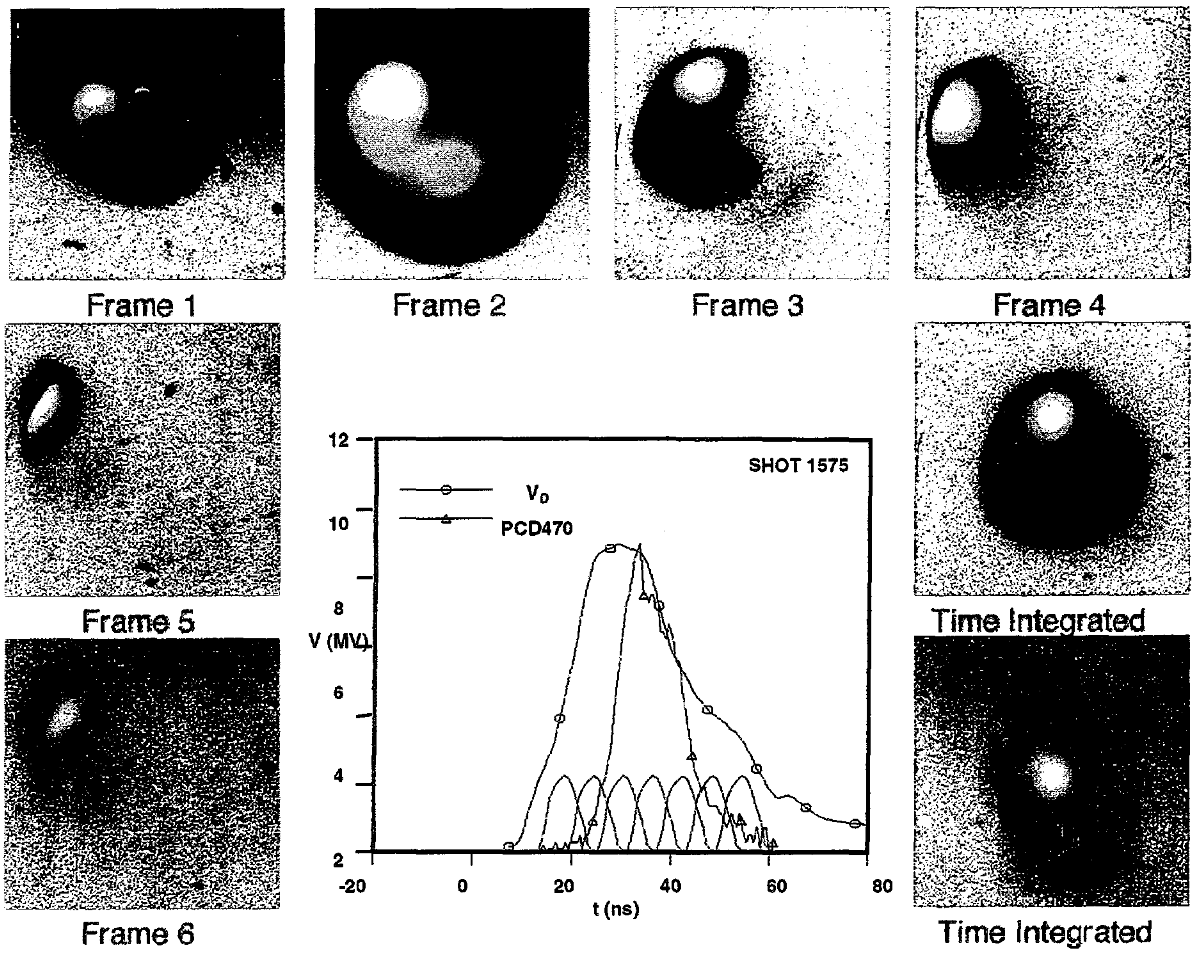

Figure 29. X-ray source evolution for a high (29 T) magnetic field, shot 1575. At 29 Tesla, the beam spot size does not grow with time. Because of a misaligned cathode tip, the halo and main beam centroids are clearly separated. The seven x-ray framing camera bias pulse timing versus the diode voltage and PCD x-ray pulse is also shown (insert). Images are uncorrected film density.

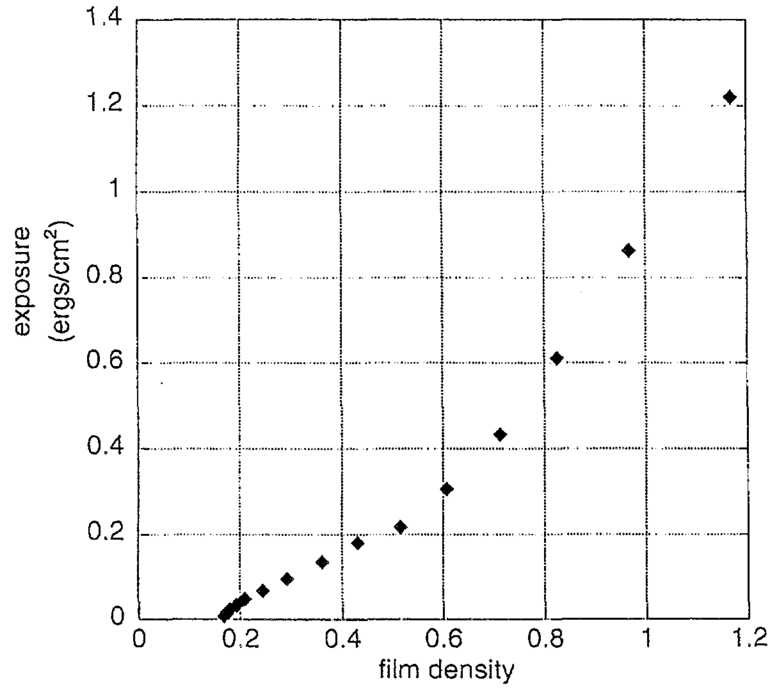

Figure 30. X-ray framing camera film calibration.

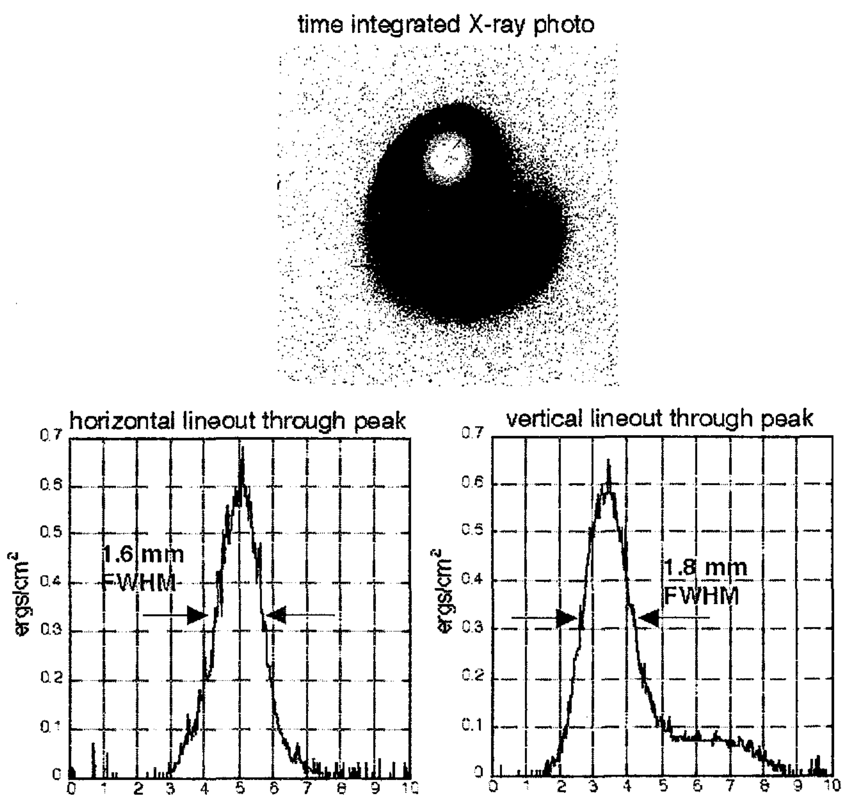

Figure 31. Time-integrated x-ray source image of Fig. 29 with magnification and film response corrections.

The finite pinhole size (Fig. 20) obviously produces some blurring of the image, and knowledge of the point spread function (PSF) of the optical system is required for the deconvolution. The PSF for a similar camera used at Sandia on another accelerator produced x-ray source[27] was calculated from a monte carlo simulation and is shown in Fig. 32. The scattered x-ray intensity is negligible, and the PSF is nearly a uniform step function with a radius of 0.16 mm. The object plane, pinholes, and image plane for the SABRE camera are somewhat different from this other camera and creates an image 3.5x larger. Thus, geometrical considerations for a linear optical system suggest an approximate PSF for the SABRE camera of a uniform step function with a radius of 0.56 mm. This was used to unfold the SABRE data with an inverse Wiener filter deconvolution applied to the image in Fig. 31. The equation used was:

$$W = \frac{F_i \bullet P^*}{|P|^2 + k}$$

where W is the Fourier transform of the corrected image, F_i is the Fourier transform of the image (with film response unfolded), P is the Fourier transform of the PSF, P* is the complex conjugate of P, and k is the noise spectrum ratio, a constant. Various constants for the noise spectrum ratio (k), and various sizes of Wiener spectrum masks were applied. Figure 33 shows a reasonable restored image using k = 0.001 and a mask (value is zero everywhere but the mask) diameter of 2.5 mm. This image gives an x-ray source FWHM size of about 1.5 mm.

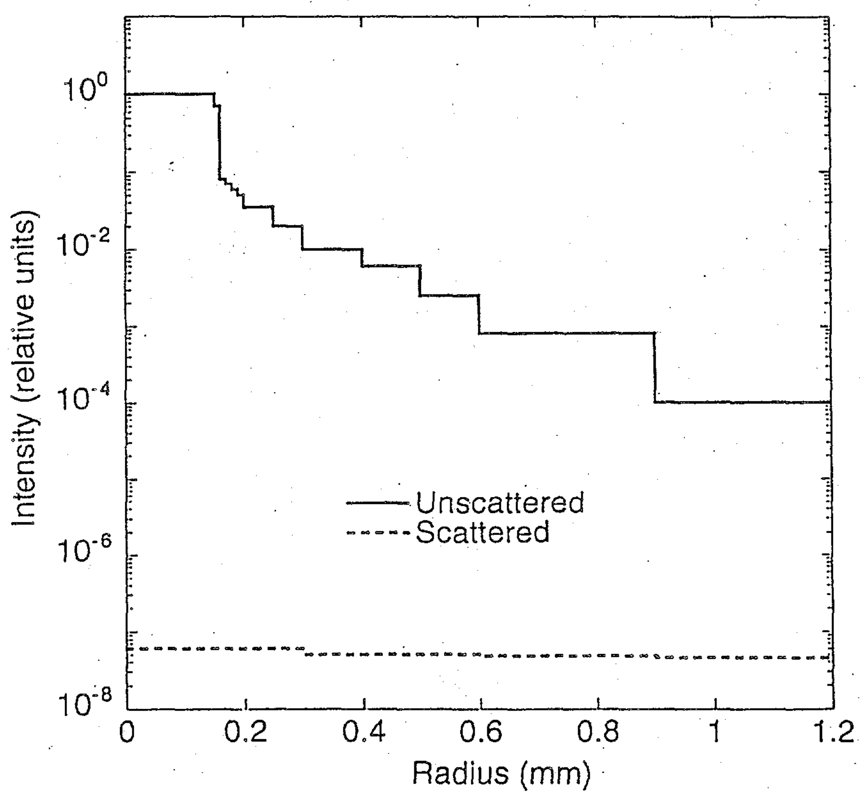

Figure 32. Point spread function of an x-ray framing camera similar to that used in these experiments.

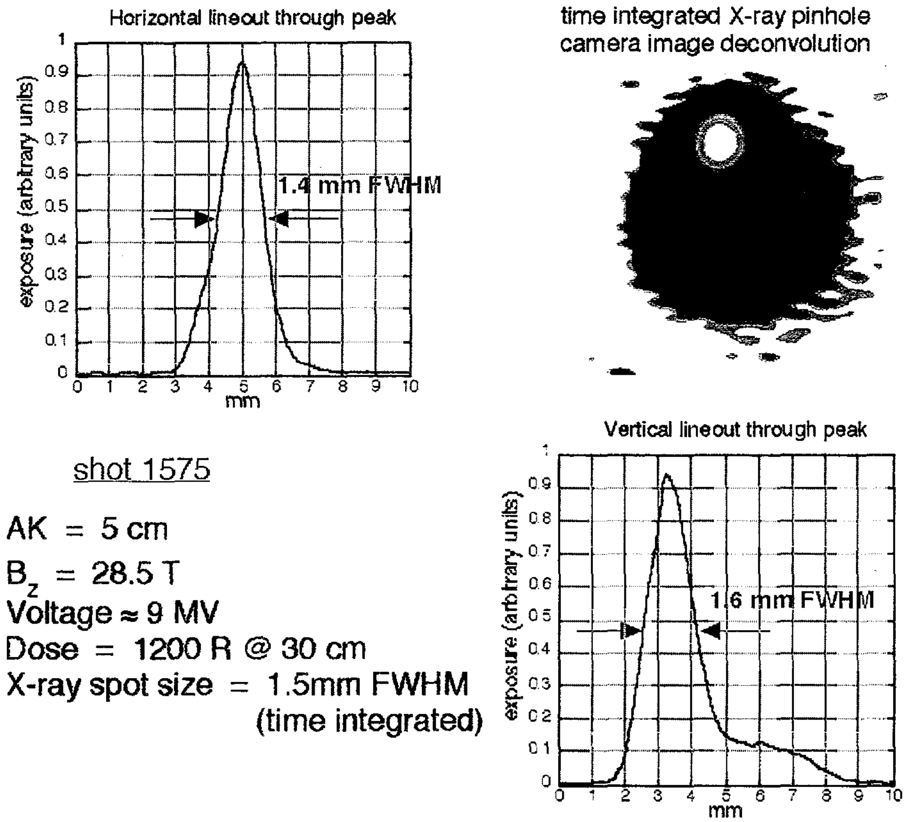

Figure 33. Time-integrated x-ray source image of Fig. 29 corrected for finite pinhole size effects. The radiation source spot has a ~ 1.5-mm FWHM.

The intense core is surrounded by a time-invariant tenuous halo. In this particular shot, the cathode needle was misaligned relative to the magnetic field axis, with the tip displaced approximately 5 mm. This source offset caused the instrument data clipping in frames 4-6. The static nature of the profile demonstrates stable operation without any of the anode or cathode plasma dynamic effects to which the technology had been feared susceptible. The halo problem may be unrelated to the ion-hose instability. With higher B_Z (> 20 T), the halo is clearly distinguished from the main beam. In addition, the location of core and halo remains unchanged in time (Fig. 29) in contrast with observations at lower fields (Fig. 28). The halo is believed principally due to emission from the needle holder and should be eliminated in a design guided by a systematic study and analysis of the transition region profile in conjunction with magnetic field shaping.

XII. Summary

An immersed diode and a high-impedance voltage adder and immersed diode were designed, constructed, and experimentally tested on the SABRE inductive voltage adder accelerator to study the potential utility of this technology for Advanced Hydrodynamic Radiography. Preshot predictions suggest this configuration should generate a very intense high-brightness electron beam of millimeter size. In the first experimental validation of the design, halo and instabilities imposed a lower limit of 2-mm x-ray source radius. A magnetic field increase to ~ 30 T mitigated the instabilities and reduced the source radius to 0.8 mm. These results are in good agreement with 2D PIC code simulations of power flow, load coupling, and intense electron beam formation and transport. 3D IVORY code simulations further explain the beam behavior as a saturating ion-hose instability. The halo, notwithstanding its low intensity, remains unexplained. It is believed, based on Sandia and Los Alamos PIC simulations, to be due to emission from the cathode tip holder. An improved design of the cathode shape near the diode should eliminate this problem. The experimental data shows promise for producing a 1-mm diameter x-ray source with reasonable extrapolations to smaller cathode tips and larger magnetic fields. The SABRE x-ray dose at 1 m is in good agreement with calculations and can be extrapolated to 1 kR for an optimally designed 12-MV, 50-ns flat-top power pulse accelerator, which would meet the national requirements for single pulse Advanced Hydrodynamic Radiography. Thus, this Technology Demonstration effort has succeeded in expanding and validating the modeling and simulation tools and has provided a solid data point which scales to full AHR parameters with a compact and inexpensive technology.

References

1. T. M. Martin, *IEEE Trans. Nucl. Sci.* **NS-16**, 59 (1969).

2. J. J. Ramirez, J. P. Corley, and M. G. Mazarakis, *Proc. 5th Int. Conf. on High-Power Particle Beams*, San Francisco (Physics International, San Leandro, CA, 1983), p. 256.

3. R. B. Miller, K. R. Prestwich, J. W. Poukey, B. G. Epstein, J. R. Freeman, A. W. Sharpe, W. K. Tucker, and S. L. Shope, *J. Appl. Phys.* **52**, 1184 (1981).

4. M. G. Mazarakis, G. T. Leifeste, R. S. Clark, C. A. Ekdahl, C. A. Frost, D. E. Hasti, D. L. Johnson, R. B. Miller, J. W. Poukey, K. R. Prestwich, S. L. Shope, and D. L. Smith, *Proc. 1987 IEEE Particle Accelerator Conf.*, Washington, DC (IEEE, New York, 1987), p. 908.

5. M. G. Mazarakis, J. W. Poukey, S. L. Shope, C. A. Frost, B. N. Turman, J. J. Ramirez, and K. R. Prestwich, *Proc. 8th Int. IEEE Pulsed Power Conf.*, San Diego, CA (IEEE, New York, 1991), p. 86.

6. D. E. Hasti, J. J. Ramirez, P. D. Coleman, C. W. Huddle, A. W. Sharpe, L. L. Torrison, *Proc. 5th Int. IEEE Pulsed Power Conf.*, Arlington, VA (IEEE, New York, 1985), p. 147.

7. L. M. Friedman and M. Ury, *Rev. Sci. Instrum.* **41**, 1334 (1970).

8. T. J. Kauppila, L. A. Builta, R. L. Carlson, D. C. Moir, and R. N. Ridlon, Los Alamos National Laboratory Report LA-UR-89-972, 1989.

9. J. Corley, J. A. Alexander, P. J. Pankuch, C. E. Heath, D. L. Johnson, J. J. Ramirez, and G. J. Denison, *Proc. 8th Int. IEEE Pulsed Power Conf.*, San Diego, CA (IEEE, New York, 1991), p. 920.

10. J. J. Ramirez, K. R. Prestwich, E. L. Burgess, J. P. Furaus, R. A. Hamil, D. L. Johnson, T. W. L. Sanford, L. E. Seamons, L. X. Schneider, and G. A. Zawadzkas, *Proc. 6th Int. IEEE Pulsed Power Conf.*, Arlington, VA (IEEE, New York, 1987), p. 294.

11. J. H. Creedon, *J. Appl. Phys.* **48** (3), 1070 (1977).

12. N. Christophilos, R. E. Hester, W. A. S. Lamb, D. D. Reagan, W. A. Sherwood, and R. E. Wright, *Rev. Sci. Instrum.* **35** (7), 886 (1964).

13. M. G. Mazarakis, R. B. Miller, J. W. Poukey, and R. J. Adler, *J. Appl. Physics* **62** (10), 4024 (1987).

14. J. W. Poukey, M. G. Mazarakis, C. A. Frost, and J. J. Ramirez, *Proc. IEEE Particle Accelerator Conf.*, San Francisco, CA (1991), p. 3059.

15. M. G. Mazarakis, J. W. Poukey, C. A. Frost, D. L. Johnson, S. L. Shope, J. A. Halbleib, K. R. Prestwich, B. N. Turman, and I. Smith, *Proc. IEEE Int. Conf. on Plasma Sci.*, Tampa, FL (1992), p. 104.

16. M. G. Mazarakis, J. W. Poukey, D. Rovang, S. Cordova, P. Pankuch, R. Wavrik, D. L. Smith, J. E. Maenchen, L. Bennett, K. Shimp, and K. Law, *in Space Charge Dominated Beams and Applications of High Brightness Beams*, edited by S. Y. Lee (AIP, New York, 1996), p. 479.

17. R. S. Coats, ATHETA/DATHETA User's Guide (Sandia National Laboratory document, Albuquerque, NM, 1995).

18. M. G. Mazarakis, J. W. Poukey, S. L. Shope, D. E. Hasti, D. L. Smith, M. D. Haworth, C. A. Frost, G. T. Leifeste, and J. S. Wagner, *Proc. IEEE Particle Accelerator Conf.*, Chicago, IL (1989), p. 1002.

19. D. B. Seidel, M. L. Kiefer, R. S. Coats, T. D. Pointon, J. P. Quintenz, and W. A. Johnson, *Proc. CP90 Europhysics Conf. on Computational Physics*, Singapore (World Scientific, Singapore, 1991), p. 475.

20. C. M. Snell, B. G. DeVolder, T. J. T. Kwan, R. J. Kares, LANL Report XPA-RN (U), 96-024.

21. B. B. Godfrey and T. P. Hughes, *Phys. Fluids* **28**, 669 (1984).

22. B. G. DeVolder, T. J. T. Kwan, C. M. Snell, LANL Report XPA-RN (U), 96-017.

23. K. G. Budge and J. S. Peery, *Int. J. Impact Engng*. **14** (1-4), 107 (1993).

24. D. D. Bloomquist, R. W. Stinnett, D. H. McDaniel, J. R. Lee, A. W. Sharpe, J. A. Halbleib, L. G. Schlitt, P. W. Spence, and P. Corcoran, *Proc. 6th IEEE Pulsed Power Conf.*, Arlington, VA (IEEE, New York, 1987), p. 310.

25. R. S. Wagner, et al., *Proc. 1992 IEEE Nucl. Sci. Symposium* **1**, 88(1992).

26. J. A. Halbleib, R. P. Kensek, T. A. Mehlhorn, G. D. Valdez, S. M. Setzer, and M. J. Berger, *IEEE Trans. Nuc. Sci.* **39**, 1025 (1992).

27. W. A. Stygar, H. C. Ives, R. P. Kensek, G. A. Mastin, B. P. Peyton, K. Allen, E. R. Brock, J. Cuny, D. L. Fehl, D. C. Ghiglia, J. A. Halbleib, V. Harper-Slaboszewicz, M. A. Hedemann, C. R. McClenahan, M. A. Palmer, P. Reyes, and P. Taylor, *Proc. Defense Nuclear Agency Instrumentation for Nuclear Weapons Effects Testing (INWET) Conf.*, edited by M. Flohr (Kaman Sciences Corp., Alexandria, VA, 1990), vol. 2, p. 3/130.

28. AWE Report AWE/HD01/B/9509/249.

29. S. Watson, private communication, May 6, 1996.

30. C. Ruiz and G. Cooper, private communication, July 1996.

31. L. G. Multhauf, N. L. Back, presentation to the Hydrotest Program Assessment Independent Consultants (HPAIC), January 29, 1992.

Distribution

3 Department of Energy
Attn: R. Staffin, DP-10
S. Kahales, DP-16
B. Hamby, DP-16
19901 Germantown Road
Germantown, MD 20585

17 Los Alamos National Laboratory
Attn: D. Wolkerstorfer
S. Younger
M. Burns
D. Prono
B. Day
M. Jones
T. Kwan
B. DeVolder
R. Kares
C. Snell
H. Agnew
D. Fulton
P. Allison
D. Moir
S. Watson
R. Carlson
K. Mueller
P. O. Box 1663
Los Alamos, NM 87545

7 Lawrence Livermore National Laboratory
Attn: L. Multhauf
M. Anastasio
G. Miller
D. Lear
L. Wiley
N. Back
G. Caparoso
P. O. Box 808
Livermore, CA 94550

3 Mission Research Corporation
Attn: D. R. Welch
T. Hughes
B. Oliver
1720 Randolph Road SE
Albuquerque, NM 87106

2 Pulse Science Inc.
Attn: I. Smith
V. Bailey
600 McCormick St.
San Leandro, CA 94577

3 Maxwell Laboratories
Attn: Y. G. Chen
R. White
R. Miller
8888 Balboa Avenue
San Diego, CA 92123

2 Naval Research Laboratory
Attn: F. Young
G. Cooperstein
4555 Overlook Ave. SW
Washington, DC 20375

1 Cornell University
Attn: D. Hammer
Lab of Plasma Studies
369 Upson Hall
Ithaca, NY 14853

1 SAIC
Attn: A. Toepfer
21098 Airpark Road SE
Albuquerque, NM 87106

1 SAIC
Attn: R. Briggs
5000 Hopward Rd., Suite 350
Pleasanton, CA 94588

Distribution (continued)

1 K. Prestwich
12201 Cedar Ridge Dr. NE
Albuquerque, NM 87112

2 Lawrence Berkeley Laboratory
Attn: S. Yu
E. Lee
1 Cyclotron Road
Berkeley, CA 94720

1 J. Leiss
Rt. 2, Box 142C
Broadway, VA 22185

1 SM Technologies, Inc.
Attn: T. Godlove
Patriot Square
10529-B Braddock Rd.
Fairfax, VA 22032

1 SLAC
Attn: W. Hermansfeldt
2575 Sand Hill Rd.
Menlo Park, CA 94025

2 Physics International Company
Attn: C. Stallings
P. Sincerny
2700 Merced Street
San Leandro, CA 94547

2 Bechtel-Nevada
Attn: D. Hays
C. Hagen
P. O. Box 98521
Las Vegas, NV 89193-8521

2 Atomic Weapons Research
Establishment
Attn: M. Goodman
D. Forster
Aldermaston, Reading RG7 4PR
Berkshire, ENGLAND

1	MS	0463	R. L. Hagengruber, 5000
1	MS	0472	J. F. Ney, 5100
1	MS	0472	A. K. Hays, 5136
1	MS	0747	R. E. Pepping, 6412
1	MS	0151	G. Yonas, 9000
1	MS	0828	R. D. Skocypec, 9102
1	MS	0819	T. G. Trucano, 9231
1	MS	1165	J. E. Powell, 9300
1	MS	1166	J. H. Renken, 9301
1	MS	1170	G. A. Zawadzkas, 9302
1	MS	1155	W. Beezhold, 9303
1	MS	1165	P. S. Raglin, 9304
1	MS	1170	L. Posey, 9305
1	MS	1178	J. J. Ramirez, 9310
1	MS	1159	M. A. Hedemann, 9311
1	MS	1168	W. B. Boyer, 9321
1	MS	1169	C. W. Cook, 9322
1	MS	1153	M. T. Buttram, 9323
1	MS	1156	R. Tachau, 9333
1	MS	1179	J. R. Lee, 9341
1	MS	1179	J. A. Halbleib, 9341
1	MS	1179	W. P. Ballard, 9341
1	MS	1179	D. E. Beutler, 9341
1	MS	1106	A. W. Sharpe, 9342
1	MS	1107	K. Mikkelson, 9342-1
1	MS	1167	E. F. Hartman, 9351
1	MS	1166	G. J. Scrivner, 9352
1	MS	1145	P. Pickard, 9360
1	MS	1141	J. W. Bryson, 9361
1	MS	1146	T. F. Luera, 9363
1	MS	1175	L.A. Miller, 9364
1	MS	1143	J. S. Philbin, 9365
1	MS	1190	D. L. Cook, 9500
1	MS	1195	J. P. Quintenz, 9502
1	MS	1178	R. Hamil, 9512
1	MS	1182	B. N. Turman, 9521
1	MS	1182	D. J. Johnson, 9521
1	MS	1182	T. J. Renk, 9521
20	MS	1193	J. E. Maenchen, 9531
1	MS	1193	J. S. Lash, 9531
1	MS	1193	M. G. Mazarakis, 9531
1	MS	1193	P. R. Menge, 9531
1	MS	1193	D. C. Rovang, 9531

Distribution (continued)

1	MS	1193	T. W. L. Sanford, 9531
1	MS	1193	S. R. Cordova, 9531
1	MS	1187	T. A. Mehlhorn, 9533
1	MS	1186	M. E. Cuneo, 9533
1	MS	1186	D. L. Hanson, 9533
1	MS	1182	D. D. Bloomquist, 9536
1	MS	1184	J. Boyes, 9539
1	MS	1184	D. L. Johnson, 9539
1	MS	1184	D. L. Smith, 9539
1	MS	1184	L. Bennett, 9539
1	MS	1186	C. L. Olson, 9541
1	MS	1186	J. W. Poukey, 9541
1	MS	1187	M. K. Matzen, 9571
1	MS	1194	D. H. McDaniel, 9573
1	MS	1181	J. R. Asay, 9575
1	MS	1196	R. J. Leeper, 9577
1	MS	1196	W. A. Stygar, 9577
1	MS	0317	J. Polito, 9800
5	MS	0899	Technical Library, 4414
2	MS	0619	Review & Approval Desk,12690 for DOE/OSTI
1	MS	9018	CTF, 8940-2